TAMPEREEN TEKNILLINEN YLIOPISTO
TAMPERE UNIVERSITY OF TECHNOLOGY

Alexey Veselov

Optical Fibers Functionally Enhanced by Photoactive Molecules

Julkaisu 997 • Publication 997

Tampere 2011

Tampereen teknillinen yliopisto. Julkaisu 997
Tampere University of Technology. Publication 997

Alexey Veselov

Optical Fibers Functionally Enhanced by Photoactive Molecules

Thesis for the degree of Doctor of Science in Technology to be presented with due permission for public examination and criticism in Sähkötalo Building, Auditorium S1, at Tampere University of Technology, on the 23rd of November 2011, at 12 noon.

Tampereen teknillinen yliopisto - Tampere University of Technology
Tampere 2011

ISBN 978-952-15-2670-1 (printed)
ISBN 978-952-15-2680-0 (PDF)
ISSN 1459-2045

Abstract

The experimental platform to study optical fibers (OFs) functionally enhanced by layers of photoactive molecules was developed. The used multimode step-index OFs were preliminary mechanically or chemically modified. Photonic crystal fibers (PCFs) were used as supplied. The photoactive layers were deposited using Langmuir-Blodgett and self-assembling monolayer (SAM) techniques. Two types of compounds were used for the fiber functionalization, porphyrin derivatives and Citrine (modified yellow fluorescent protein). This work is the first demonstration of SAM deposition of porphyrin derivatives on conventional OFs and inside the channels of PCFs, as well as Citrine SAM deposition on OFs. The developed experimental optical setup together with installed modified OFs rendered possible: i) to deliver the excitation light to the photoactive molecules, and ii) to collect the fluorescence and deliver it to the measuring system. Moreover, the same experimental system was used to optimize SAM process. It can also be used for real-time monitoring of SAM deposition of any type of photoactive molecules.

The light guided by conventional multimode step-index fibers can only interact with molecules on its surface if the cladding layer is essentially thinned or removed completely. This can be done either by tapering or chemical etching of an OF. The optimum geometries for the tapered regions were determined by two methods based on fluorescence intensity measurements of the molecular films. The optimum tip diameter of a tapered OF was found to be $35 - 48$ μm for the fibers with 105 μm core and 125 μm cladding diameters. For the etched OFs the reasonable tip diameter was 70 μm for the same fiber, and sufficient tip length was 2.5 mm.

The modified OFs were tested in sensor applications for detecting pH, Ca^{2+}, and volatile organic compounds (diethylamine was used in this study). A reasonable reproducibility of pH measurements was demonstrated for OF sensor with free-base porphyrin probe in the pH range of $0.6 - 3.8$ and for Citrine probe in the pH range of $6.5 - 9$. The sensitivity of Ca^{2+} ion sensor with Citrine SAM was on the level of a few tens of μM and diethylamine was detected at a few mM concentration using Zn-porphyrin OF sensor.

The strongest fluorescence response of functionalized OFs in typical sensor application

configuration was obtained for hollow core PCFs. The photoactive SAMs were deposited inside the light guiding channels, thus providing the most efficient excitation and fluorescence collection among the studied fibers. These OFs can be used in applications that require high sensitivity and the smallest amount of analyte. Alternatively, chemically etched conventional OFs are relatively easy to produce and functionalize. They provide reasonably high efficiency of SAM excitation and fluorescence collection and can be successfully used in less demanding optical sensor applications.

Preface

This work was carried out at the Department of Chemistry and Bioengineering, Tampere University of Technology during 2008-2011.

First of all, I would like to express my gratitude to my supervisor, the Head of the group of Ultrafast Spectroscopy, Prof. Nikolai Tkachenko for trusting in me, giving me the possibility to work in his research group and write this Thesis. I want to thank Prof. Tkachenko for all his help both in the theoretical and practical issues of physics and especially, chemistry (the field which I was not quite familiar with before coming here). I would also like to thank Prof. Tkachenko for his help during my first months of stay in Tampere to adopt to this new life in Finland. I would also like to thank my second supervisor, the Head of the Laboratory of Chemistry, Prof. Helge Lemmetyinen for the opportunity to work in his research group equipped with state of the art instruments and for believing in my skills to finish the Thesis.

I would also like to thank Dr. Alexander Efimov for all the used compounds which were synthesized in the Synthetic Chemistry group and for his very helpful advices in theoretical and practical matters of chemistry, and life situations. Besides, I want to thank Dr. Vladimir Chukharev for all his help and useful advices in practical issues in the ultrafast spectroscopy lab. My warmest thanks go also to all the co-authors of the papers, Prof. Mircea Guina, Prof. Oleg Okhotnikov, C. Thür, A. Chamorovsky, and B.G. Abraham.

For the pleasant work atmosphere I am grateful to all the staff at the Laboratory. Special thanks go to my roommates, Antti Tolkki, Rajeev Dubey, Somnath Dey, and Ali Al-Subi.

My deepest thanks are for my parents, I always felt their support behind my back even in dark hours. I would also like to thank my girlfriend and my friends in Saint-Petersburg for their permanent support and trust in me.

The financial support from the Academy of Finland and the National Doctoral Programme in Nanoscience (NGS-NANO) is gratefully acknowledged.

Tampere, August 2011

Alexey Veselov

Contents

List of Publications

The Thesis is based on the following publications, hereafter referred to by their Roman numerals:

I. **Photochemical properties of porphyrin films covering curved surfaces of optical fibers.**

A. Veselov, C. Thür, V. Chukharev, M. Guina, H. Lemmetyinen, N.V. Tkachenko.

Chem. Phys. Lett., *471*: 290–294, **2009**.

II. **Photochemical properties of porphyrin films covering surfaces of tapered optical fibers.**

A. Veselov, C. Thür, V. Chukharev, M. Guina, H. Lemmetyinen, N.V. Tkachenko.

Proc. of SPIE, 7503: 75031K1–75031K4, **2009**.

III. **Acidity sensor based on porphyrin self-assembled monolayers covalently attached to the surfaces of tapered fibres.**

A. Veselov, C. Thür, A. Efimov, M. Guina, H. Lemmetyinen, N.V. Tkachenko.

Meas. Sci. Technol., *21*: 115205–115215, **2010**.

IV. **Self-assembled monolayers (SAMs) of porphyrin deposited inside photonic crystal fibre (PCF).**

A. Veselov, C. Thür, A. Efimov, M. Guina, H. Lemmetyinen, N.V. Tkachenko.

Phys. Status Solidi A, 208 (8): 1858–1861, **2011**.

V. **Photochemical properties and sensor applications of modified Yellow Fluorescent Protein (YFP) covalently attached to the surfaces of etched optical fibres (EOFs).**

A. Veselov, B.G. Abraham, M. Karp, H. Lemmetyinen, N.V. Tkachenko.

Anal. Bioanal. Chem., submitted.

Abbreviations and symbols

APTMS	3-aminopropyltrimethoxysilane
BFT	bare fiber terminator unit
BS	beamsplitter
CCD	charge-coupled device, an image recording detector
CFD	constant fraction discriminator
DM	dichroic mirror
DEA	diethylamine
EOF	etched optical fiber
EDTA	ethylenediaminetetraacetic acid
EW	evanescent wave
F	filter
FLM	fluorescence lifetime microscopy
GFP	green fluorescent protein
HOMO	highest occupied molecular orbital
HCPBGF	hollow-core photonic bandgap fiber
HF	hydrofluoric acid
HTOF	hyperbolically tapered optical fiber
ITO	indium tin oxide
ISRTOF	inverse square root tapered optical fiber

ISTOF	inverse squared tapered optical fiber
LB	Langmuir-Blodgett deposition method
LbL	layer-by-layer deposition method
L	lens
LTOF	linearly tapered optical fiber
LoTOF	long tapered optical fiber
LUMO	lowest unoccupied molecular orbital
mma	mean molecular area
M	mirror
MTESP	mono(triethoxysilane) porphyrin
MCA	multichannel analyzer
NA	numerical aperture
ODA	octadecylamine
PFP	5,10,15,20-tetrakis(pentafluorophenyl)porphyrin
PBS	phosphate buffered saline
PD	photodetector
PMT	photomultiplier tube
PCF	photonic crystal fiber
SAM	self-assembled monolayer deposition method
STOF	short tapered optical fiber
SPAD	single-photon avalanche diode
SCPCF	solid-core photonic crystal fiber
sulfo-SMCC	sulfosuccinimidyl 4-[N-maleimidomethyl]cyclohexane-1-carboxylate

TOF	tapered optical fiber, taper
TC	telescope condenser
TCSPC	time-correlated single photon counting
TAC	time-to-amplitude converter
TIR	total internal reflection
VSI	vertical scanning interferometry
VOC	volatile organic compound
YFP	yellow fluorescent protein
A	absorbance
α	angle between the incident beam and normal to the core-cladding interface in bare fiber
α_C	critical angle for straight part of a tapered optical fiber
$\alpha(z)$	angle between the incident beam and normal to the core-cladding interface in the tapered region
$\alpha_C(z)$	critical angle for coned part of a tapered optical fiber
a_i	radius of the fiber core in the beginning of tapered region (highest value)
a_o	radius of the fiber core in the end of tapered region (lowest value)
$a(z)$	radius of the fiber core in the tapered region
b	distance between the centers of successive holes in a photonic crystal fiber
δ	distance from the core-cladding interface
d_p	penetration depth parameter
Γ	tapering angle
L	length of the tapered region
n_{cl}	refractive index of the cladding layer

n_{co}	refractive index of the core
π	surface pressure
V	waveguide parameter
w	mode field diameter

1 Introduction

Study of the light interaction with novel materials is a long-term interdisciplinary research topic in the field of natural sciences. Fast developments in this field are rendered possible because of the invention of new types of materials and techniques to interact with light on micro- and nanoscales.

Photoactive molecules (and layers of photoactive molecules) are among the most rapidly developing topics in the fields of physics, chemistry, and photochemistry. New photoactive materials based on novel molecular and supramolecular systems with specific functions, such as efficient light harvesting and photoinduced charge transfer are under active development [1, 2]. On the other hand, recent tremendous progress in fiber optics and photonics opens out new perspectives on light manipulation as a useful tool to enhance the interaction with various molecular [3] and atomic [4] systems and delivering photons to a particular photoactive object [5], nanostructures [6], or even a single particle [7]. Combination of developments in these two vastly growing areas – development of novel photoactive materials and new kinds of optical fibers – hold much promise for new exciting discoveries and technological advances.

This Thesis is dedicated to the investigation of microstructured optical fibers functionally enhanced by the layers of photoactive molecules, namely porphyrins and fluorescent proteins. Developed experimental optical setup with installed modified fibers was used to deliver excitation light to the molecular layers, collect the layers emission and deliver it to the measuring system. The main aims of the research work were: i) to determine optimum geometries for the fiber-molecular film interface, ii) to study and tune properties of the molecular films deposited on tapered and etched fibers, and inside the channels of photonic crystal fibers, and iii) to study sensor applications of the functionalized fibers.

2 Background

2.1 Optical fibers. Evanescent field description

Optical fibers are waveguides, which are usually made of some kind of glass, can potentially be very long (hundreds of kilometers), and are fairly flexible. The most commonly used glass is silica (quartz glass, amorphous silicon dioxide, SiO_2), either in pure form or with some dopants. Silica is used because of its properties, which are: extremely low light propagation losses, high mechanical strength against pulling and bending, and high availability in nature. A typical optical fiber consists of three layers (Figure 2.1): optical fiber core, cladding layer and buffer layer. The central region is the core, which is the light guiding part of the fiber. The core is surrounded by the cladding, that is in turn surrounded by a protective buffer. Within the core the refractive index profile can be uniform (*step profile*) or graded (*graded profile*), and the cladding index is typically uniform. The waveguiding of an optical fiber is rendered possible by total internal reflection (TIR) on the boundary between the fiber core which has higher refractive index and the cladding layer which has a lower refractive index. The buffer layer is almost optically isolated from the core. In this work, optical fibers which have step-index profiles of the refractive index were used.

Optical fibers can be divided into two subclasses which are *multimode* waveguides (typically core diameter ranges from 12.5 to 110 μm) and *single-mode* waveguides (core

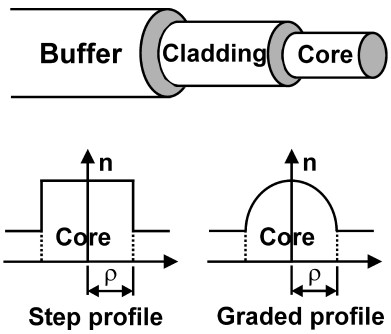

Figure 2.1: Nomenclature and profiles for typical optical fibers; ρ is the core radius.

diameter is typically between 2 and 8 μm) [8]. This division is accomplished according to the so-called *waveguide* or *fiber parameter* V which is defined as [8]:

$$V = \frac{2\pi\rho}{\lambda}\sqrt{n_{co}^2 - n_{cl}^2} \tag{2.1}$$

where ρ is the core radius, is λ the wavelength, n_{co} and n_{cl} are the refractive indices of the core and cladding, respectively. For V value below 2.405, a fiber supports only one mode per polarization direction (and therefore, it is called monomode or single-mode optical fiber), whilst a waveguide is said to be multimode when $V > 2.405$. Multimode optical fibers were used in studies presented in this Thesis.

Another parameter which can be used to characterize optical fibers is the *mode diameter, w* (or *mode field diameter*) which is defined as [9]:

$$w \approx \rho\left(0.65 + \frac{1.619}{V^{3/2}} + \frac{2.879}{V^6}\right) \tag{2.2}$$

This equation shows that the mode diameter becomes smaller for higher frequencies, which have higher V values. The equation is fairly accurate for V values between 0.8 and 2.5. In the multimode range ($V > 2.405$), it applies to the fundamental mode. An example of a standard single-mode fiber is SMF-28 (from Corning Inc.) which is commonly used in optical communications in the 1.3 and 1.5 μm wavelength region. It has a core diameter of 8.2 μm, thus having the mode field diameters approximately 9.2 and 10.4 μm at 1310 and 1550 nm, respectively.

When a ray of light undergoes TIR at the interface of two media having different refractive indices, the standing wave along the fiber optical axis is produced. At the core-cladding interface the standing wave has finite electric field amplitude, and since the field cannot go to zero instantly, it decays exponentially into the lower index cladding layer according to [10]:

$$E = E_0 \exp\left(-\delta/d_p\right) \tag{2.3}$$

where δ is the distance from the core-cladding interface and d_p is a *penetration depth* parameter. This field is called the evanescent wave (EW) field. The penetration depth determines the distance from the core-cladding interface where EW decays e-times [10]:

$$d_p = \frac{\lambda}{2\pi\sqrt{n_{co}^2 \sin^2\alpha - n_{cl}^2}} \tag{2.4}$$

where α is the angle between the incident beam and normal to the interface. Substituting

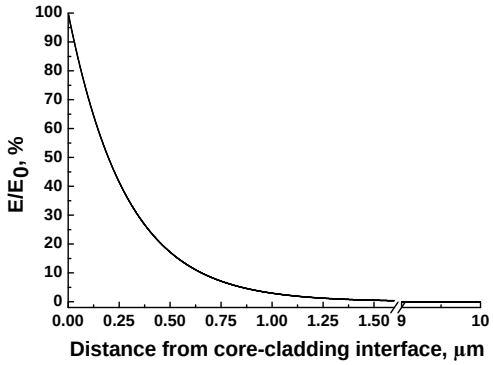

Figure 2.2: Evanescent wave decay curve (from the core-cladding interface to the cladding layer) plotted for multimode optical fiber AFS 105/125 Y (Thorlabs) for $\alpha = 89°$ and $\lambda = 430$ nm.

eq. (2.4) into (2.3), the dependence of the ratio of EW field value to EW field maximum at core-cladding interface on the distance from the core-cladding interface can be plotted. Figure 2.2 presents this dependence for standard multimode fiber AFS 105/125 Y from Thorlabs ($n_{co} = 1.48$ and $n_{cl} = 1.46$ at $\lambda = 430$ nm) assuming $\alpha = 89°$.

Typical thickness of the cladding layer of commercially available multimode fibers is 10 – 20 μm, and if a layer of photoactive molecules is deposited on the surface of cladding layer there will be no interaction of the light propagating in the fiber with the molecular layer, as it is clearly seen from Figure 2.2. For most of commercially available fibers the buffer layer (see Figure 2.1) can be removed relatively easy since it is made of material different from that of the core and cladding layer. However, the cladding layer and the core are made of the same material, silica, with different doping, and cladding layer cannot be removed easily from the core. In order to utilize the evanescent field to probe the photoactive molecules deposited on fiber surfaces by the light propagating in the fiber core (e.g. for chemical or biological sensing applications), the cladding layer has to be made significantly thinner since light does not penetrate deep into it. The photoactive molecules can be deposited on the fiber core end-face [11, 12], directly on the core-air interface of de-cladded fiber [13–15] or etched fiber [12, 16, 17], or on the core-cladding interface of sufficiently tapered fiber [12, 18]. In this Thesis, tapered and etched multimode optical fibers were studied.

2.1.1 Tapered (TOFs) and etched optical fibers (EOFs)

One of the common approach to make the cladding layer thinner is to apply fiber tapering procedure. When the optical fiber is sufficiently tapered, the cladding layer thickness

becomes comparable with the penetration depth of EW field, d_p, thus enhancing the interaction of the evanescent field with the outer medium (e.g. a molecular film of a photoactive compound deposited on the surface of tapered fiber) so that small changes of the outer medium can modulate the transmission properties of the taper.

There are two basic concepts used to manufacture tapered optical fibers (TOFs): heating and pulling optical fiber apart, and using chemical etching. Heating can be achieved with, for instance, gas flame [18–20], ceramic heater [21], or with intensive laser beam [12, 22, 23]. In this Thesis, the TOFs were manufactured using heating and pulling technique with gas flame and ceramic heater.

In order to manufacture de-cladded optical fibers with very short translational stages in radius profiles, two basic methods can be applied: chemical etching and polishing D-shape technique. The latter is usually applied for polymer optical fibers for which the first technique cannot be utilized. The polishing method is based on mechanical removal of the cladding layer with a polishing wheel and grease [24–26]. With this method, any type of surfaces can be achieved: fiber can be de-cladded or even the core diameter can be reduced.

The other technique is based on chemical etching of quartz fibers with hydrofluoric acid, HF. Using this method, even sub-micrometer scale tapered fibers can be achieved [12]. This technique was used in this Thesis to obtain etched optical fibers (EOFs). The technique was described in more details elsewhere [27, 28]. In order to prevent evaporation of extremely toxic HF, the protection layer of solvent between hydrofluoric acid and air can be injected. Different protecting solvents give various cone angles of taper as was demonstrated, e.g., by Hoffmann and co-workers [29]. The main advantages of EOFs over TOFs are easier procedure of manufacturing and shorter length of translational stage that is required for the evanescent field to reach a fiber surface.

2.1.2 Photonic crystal fibers (PCFs)

Photonic crystal fibers (PCFs) are optical fibers with a built-in microstructure consisting of small air holes in glass [30]. PCFs are in practical usage since 1996, nevertheless examples of photonic crystals can be found in nature, e.g. butterfly wings [31], peacock feathers, beetles, birds, mammals or even plants [32]. The waveguiding properties of PCFs are rendered possible not by a spatially varying glass composition but from an arrangement of very tiny and closely spaced air holes which go through the whole length of fiber.

Nowadays, there is a large variety of PCFs and techniques to manufacture them. Fig-

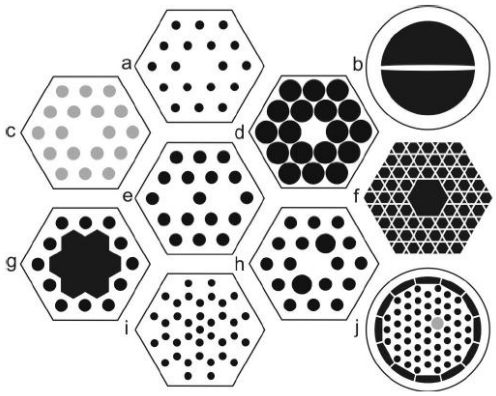

Figure 2.3: Sketches of different types of PCFs. The black regions are hollow, the white regions are pure glass, and the grey regions are doped glass. (a) Endlessly single-mode solid-core PCF. (b) Nanoweb fiber (not a PCF). (c) All-solid-glass PCF with raised-index doped glass strands in the cladding. (d) Solid core photonic crystal fiber (SCPCF). (e) Dual-core PCF. (f) Kagome hollow-core PCF. (g) Seven-cell hollow-core PCF. (h) Birefringent PCF. (i) Carbon-ring structure for photonic bandgap guidance. (j) Double-clad PCF with off-set doped lasing core and high numerical aperture inner cladding for pumping (presented with the permission from IEEE. Copyright © 2006, IEEE [33]).

ure 2.3 shows just a few sketches of various types of PCFs that can be produced [33]. One of the widely used technique to manufacture PCFs, is drawing (or stacking) process described in more details elsewhere [30, 34, 35]. In the first stage of the process, a scale model of the fiber (preform) is created which has typical dimensions of a few centimeters. The preform is then heated and pulled (drawn) stretching it into a thin strand whose cross section is a scaled-down version of the preform. This gives an opportunity to create several hundreds of meters or even kilometers of PCFs with a given cross-sectional structure. Another methods of PCF manufacture are extrusion [36–39], sol-gel casting [40], injection molding [39], and drilling [35]. The extrusion allows to fabricate structures which are not readily made by the stacking process. In this technique, the molten glass is forced through a die containing a suitably designed patterns of holes. Extrusion allows fiber to be drawn directly from bulk glass. However, this method is not suitable for silica (because the materials used in this technique cannot withstand 2000° C processing temperatures), and it is used to prepare PCFs from compound silica glasses [36], tellurites [37], chalcogenides [38], and polymers [39]. In this Thesis, hollow-core photonic bandgap fibers (HCPBGFs) and solid-core photonic crystal fibers (SCPCFs) were utilized (schematic structures of the fibers are shown in Figure 2.4).

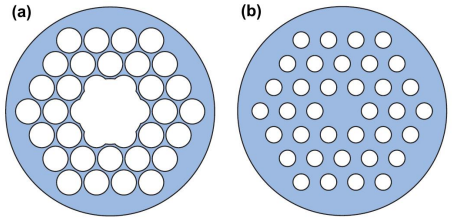

Figure 2.4: Examples of PCFs. (a) Hollow core photonic bandgap fiber (HCPBGF). (b) Solid-core photonic crystal fiber (SCPCF).

PCFs having two-dimensional periodicity in cladding structure (as in Figure 2.4a) were first described by Knight and co-authors in 1998 [41]. The cross-section is a periodic array of air holes running through the whole length of the fiber which is also referred to as HCPBGF. The second type of PCFs which was used in this Thesis, is an index-guiding photonic crystal fiber in which the periodic structure is not employed for its bandgap, but to form an effective low-index cladding around the core. This type of fibers is also referred to as SCPCFs (see Figure 2.4b) [42]. In this way, it is possible to achieve better optical confinement than in traditional optical fibers.

The total internal reflection (TIR) is not possible in HCPBGFs, since the cladding refractive index is higher than that for air. The light guidance is rendered possible by the Bragg scattering so that the light at defined stop bands is prohibited from propagation in the photonic crystal cladding and confined within a central defect. Only certain wavelength bands are confined and guided through the fiber. In HCPBGFs, the photonic crystal cladding acts as a mirror, more than 99% of optical power is located in air (not in glass) [43]. Therefore, light with wavelengths corresponding to the bandgaps cannot escape the core and it is guided along the fiber with low losses. In SCPCFs (see Figure 2.4b) the index guiding is employed. The light is guided since the cladding refractive index is smaller than that of the solid core. In the limit of short wavelengths $\lambda \ll b$ (where b is the distance between the centers of successive holes), the ray-optics limit applies and the light is guided by TIR remaining almost entirely within the dielectric material.

2.2 Methods of molecular film deposition

There is a large variety of methods which can be used to deposit layers of photoactive molecules on a glass surface. The most commonly and widely used deposition techniques providing accuracy in the layer thickness at the molecular level are: electrostatic layer-by-layer (LbL) deposition [44, 45], Langmuir-Blodgett (LB) film deposition [46, 47], and self-assembled monolayer (SAM) by covalent bonding to the surface [48, 49].

Electrostatic layer-by-layer (LbL) deposition

Electrostatic LbL deposition of multilayer films involves the construction of complex composite materials with nanoscale precision in film thickness, enabling the development of novel structures and devices. The technique was suggested by Iler [50] in 1966, and then rediscovered by Decher et al. [44] in the early 1990s. The LbL electrostatic adsorption process has been in active development during the past two decades. The technique is based on the successive deposition of oppositely charged layers of molecules (or particles) with electrostatic attraction being the driving force to form stable multilayer films. The main advantage of the method is its relative simplicity. Wide range of materials can be employed in the assembly process from charged polymers ("polyelectrolytes" or "poly-ions") [51] to proteins [52], dyes [53], and semiconductor nanoparticles [54]. The technique suggests the possibility of designing ultrathin ordered films in the range of 5 – 1000 nm with a precision better than 1 nm.

Langmuir-Blodgett (LB) film

Deposition technique of LB films involves the vertical movement of a solid substrate through a monolayer formed at water-air interface. Firstly, a monolayer of amphiphilic molecules (that is also called Langmuir layer) is formed at the water-air interface of a Langmuir trough. This is followed by the transfer of the layer onto a solid substrate by slow movement of the substrate through the molecular monolayer. The substrate can be either of hydrophilic or hydrophobic nature, which determines the direction, upstroke or downstroke, in which the deposition takes place. In this Thesis, the used samples were hydrophilic and the monolayers were deposited in the upstroke motion.

After spreading a solution of amphiphilic molecules onto the subphase in the trough, the layer of molecules is then compressed (with moving barriers) until a quasi-solid one molecule thick layer is formed. The compression system of the trough is coupled to a microbalance which continuously monitors the surface pressure, π. A typical depen-

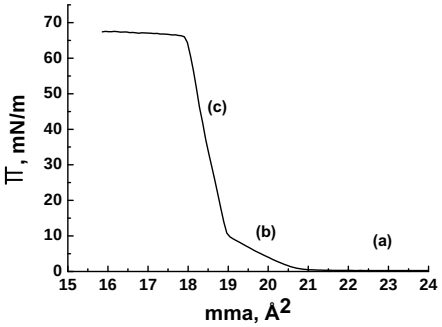

Figure 2.5: Isotherm of octadecylamine (ODA) on phosphate buffer subphase (pH 7).

dence of the surface pressure, π, on the mean molecular area (mma) (or isotherm) for octadecylamine (ODA) is presented in Figure 2.5. It clearly shows three distinguishable regions denoted in the Figure as (a), (b) and (c). The (a) region corresponds to the so-called "gaseous" phase when amphiphilic molecules are relatively far apart from each other, experience little interaction and thus, randomly distributed on the subphase surface. Then, when mma decreases, the distances between molecules in the layer on air-subphase interface decrease, the molecules start to cover most of the surface, and therefore, the surface pressure increases. This part of isotherm is referred to as "liquid" phase (region (b) in Figure 2.5). Finally, there will be a point on the isotherm when molecules are so closely packed that even small changes on barrier displacements (or equivalently, mma) would cause drastic variations in the surface pressure, which corresponds to "solid" state (region (c) in Figure 2.5). When barriers move further towards each other, there is a point on the isotherm when the distance between molecules in a layer cannot decrease any more, and the monolayer becomes unstable and collapses. It corresponds to the part of isotherm at mma smaller than 18 Å^2 in Figure 2.5.

The next step is the transfer of monolayer from the trough to a substrate, which is done by moving the substrate slowly through the Langmuir layer in upward or downward directions. The transfer process can be repeated few times to deposit multilayer films. For repeating multilayer films three types of molecular alignment in the layers can be distinguished. X-type of films is obtained when the monolayer is transfered only on the down-stroke deposition, thus resulting in out-of-substrate orientation of the hydrophobic end of the amphiphilic molecules in all layers. Z-type of multilayer films is formed in upstroke deposition only and the molecules are ordered with hydrophobic ends toward the substrate. However, the most common type of LB films is Y-type, which is achieved in sequential down- and upstroke deposition, and results in alternating layers with ori-

entations of hydrophobic end out from and toward the substrate, respectively. In this Thesis, only monolayer films were deposited in upstroke direction, which can be formally attributed to Z-type films.

Self-assembled monolayer (SAM)

The field of SAMs has witnessed growing increase of its development during the last 30 years. First publication on the preparation of a monomolecular layer by adsorption (self-assembly) of a surfactant onto a clean metal surface dates back to 1946 [55]. Nowadays, SAM methods are used (and they are still under development) to deposit different types of organic [55] and bio-organic molecules [56] on different types of surfaces.

The SAM procedure by covalent bonding to the surface consists of a few steps which are thoroughly described in a number of review articles [49, 55]. The molecules designed for SAM technique must have a special terminal group responsible for bonding to a surface. The self-assembly takes place in solution, and the first step is the solution transport of adsorbate molecules to the substrate-liquid interface that is conducted via the combination of diffusive and convective transport. This is followed by the adsorption of SAM molecules on the substrate with some adsorption rate. Generally, the overall dynamics of this step of the SAM process may be diffusion-controlled, adsorption-rate controlled, or in an intermediate mixed-kinetic regime. The next step is the molecular monolayer organization on the substrate surface. At the very beginning of this step, the molecules are adsorbed and distributed randomly on the surface of the solid substrate, but the final film evolves to closely packed molecular monolayer with relatively uniform molecular orientation and conformation. In this Thesis, the molecular bonding to the substrate is of covalent type.

There is a large amount of molecules which can be deposited on different solid substrates using SAM technique. Even multilayer structures can be formed with SAM method [55]. One of the typical examples is the deposition of alkylthiols (–SH group) on gold, that can be gold nanoparticles [57] or gold crystals [58]. Another examples of SAM films are adsorption of: *n*-alkanoic acids (–CO_2H group) on aluminum oxide, Al_2O_3 [59], fatty acids on silver oxide, AgO [60], and silane-based SAMs on silicon oxide, SiO_2 surfaces [61].

LB and SAM methods were applied in this Thesis to attach porphyrins and proteins to various optical fiber surfaces. When comparing LbL, LB and SAM deposition methods, it is worth to mention that all of these techniques allow to deposit big organic and bio molecules, as well as nanoparticles. Also polymer films can be deposited by LB and LbL

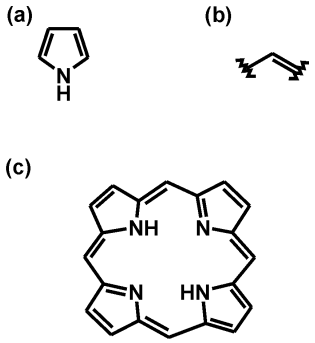

Figure 2.6: (a) Pyrrole unit, (b) methine bridge, and (c) porphin molecular structure [62].

methods. The LbL deposition is specifically advantageous for multilayer film deposition. Multilayer deposition is also possible with LB technique, but rather difficult with SAM method.

The uniform orientation of deposited molecules in a layer can be obtained with LB and SAM methods but not with LbL. The main advantage of LbL technique is its simplicity and relatively short time of deposition, whilst the preparation of molecular films with LB and SAM methods is more time consuming. An important practical advantage of SAM and LbL method is that layers can be deposited on rough surfaces and even inside micro cavities. This property of the SAM technique was used in this Thesis to deposit SAM inside the channels of PCFs.

2.3 Porphyrin and Yellow Fluorescent Protein (YFP) molecular films

Porphyrin

Porphyrins consist of four conjugated pyrrole units linked together by methine bridges [62]. In the simplest case of unsubstituted free-base porphyrin (which is also referred to as porphin), two of central nitrogen atoms bind hydrogens (see Figure 2.6). Porphyrins are able to bind various metals in its central cavity and in this case, spectroscopic properties of metal-substituted porphyrins change relative to those of free-base porphyrin. Because of the highly π-conjugated macrocyclic structure (22 π-electrons), porphyrins have strong light absorbing character in the visible region.

Porphyrins have strong absorption band with molar absorption coefficient $\varepsilon > 350000$ $M^{-1}cm^{-1}$ (called Soret band) in 410 – 450 nm wavelength range and four

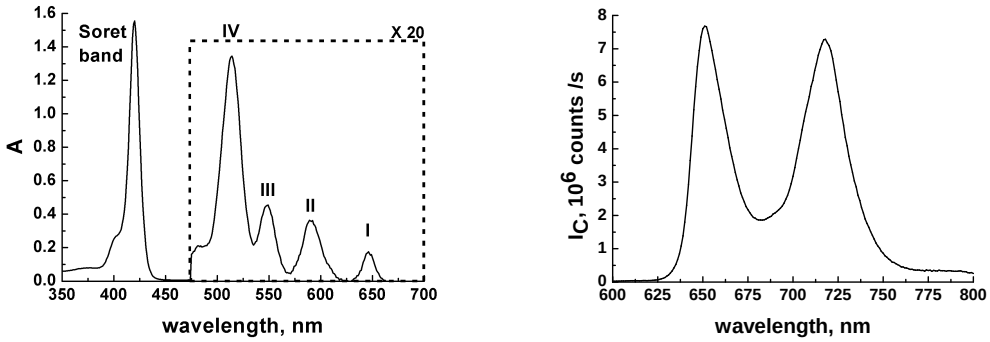

(a) (b)

Figure 2.7: (a) Absorption and (b) emission spectra of the solution of 4 μM tetraphenylporphyrin in toluene. The Q-band region, 480 – 700 nm, is magnified 20 times for better presentation.

weaker absorption bands (called Q-bands and numbered from higher wavelengths) in the wavelength region 450 – 700 nm (Figure 2.7a). The Soret band corresponds to the pure electronic transition between HOMO and LUMO+1, while the first and third Q-bands correspond to the pure electronic transitions between HOMO and LUMO, and HOMO−1 and LUMO, respectively. The second and fourth Q-bands correspond to transitions between the same HOMO and LUMO levels as first and third Q-bands, respectively, but with changes in the vibrational quantum numbers [62, 63]. Typical emission spectrum of free-base porphyrin on the example of tetraphenylporphyrin is shown in Figure 2.7b. There are two maxima, at around 650 and 720 nm with the one at 650 nm corresponding to LUMO – HOMO radiative transition.

Porphyrin and its derivatives are known to play an important role in some biological processes such as photosynthesis, dioxygen transport and its storage [64, 65], and in artificial energy and electron transfer systems [66, 67]. Besides, porphyrin is widely utilized in different sensor applications, very few examples of which can be found in [15, 68–71].

There are various techniques available to attach molecular layers of porphyrins to different kinds of substrates. One method which was utilized to prepare samples for the studies depicted in this Thesis, is SAM deposition technique. SAMs of porphyrins on glass surfaces are usually prepared in two steps. Firstly, the substrate is modified with active molecules, that can be, for instance, 3-aminopropyltrimethoxysilane (APTMS). APTMS has silane "head" that covalently attaches to the glass surface (first step), and amine "tail" is used then to covalently attach some other molecules, e.g. porphyrins

(second step). Free-base and metallated porphyrins were deposited with SAM method on various types of surfaces such as glass and quartz surfaces [72, 73], and indium tin oxide (ITO) [74–76]. Different environmental conditions and various deposition times were applied during the SAM deposition of porphyrins. The activation time (first step) varied between 1 hour [72] and 20 hours [77, 78], and the surface functionalization with porphyrin time varied between 1 hour [72] and 20 hours [74, 75]. Porphyrin solutions in various solvents with different reaction temperatures were used, for example toluene at 95 – 105 °C [75, 79], tetrahydrofuran at 60 °C [73], or dichloromethane at 25 °C [80].

Another technique which was utilized in this Thesis to deposit molecular layers of 5,10,15,20-tetrakis(pentafluorophenyl)porphyrin (PFP), is LB method. PFP is not amphiphilic molecule by itself and therefore, in order to be deposited as a film by LB method it is mixed with matrix amphiphilic molecules, such as ODA. A unique property of PFP in solid films is that it retains relatively long lifetime of the singlet excited state of a few nanoseconds even at concentrations of 10 mol-% and higher [81]. Moreover, in sharp contrast to other porphyrin LB films (for instance, tetraarylporphyrins), the fluorescence lifetime of PFP/ODA films increases with concentration (in the concentration range 0.1 – 50 mol-%). The high fluorescence efficiency of PFP films makes them an attractive candidate for sensing applications relying on fluorescence labels [82, 83].

Yellow Fluorescent Protein (YFP)

Green Fluorescent Protein (GFP) was firstly isolated from jellyfish *Aequorea victoria* and has attracted considerable interest due to its unusual fluorescence properties [84]. Discovery and development of GFP was awarded The Nobel Prize in Chemistry in 2008. At present various modifications of GFPs exist with a range of available emission wavelengths and other interesting properties which make them attracting candidates for optical sensor applications [85]. In this Thesis, a genetic variant of GFP, Yellow Fluorescent Protein (YFP) was used to study applicability of developed approach to fabricate optical fiber sensors based on SAMs of proteins.

The main advantage of fluorescent proteins over porphyrins in fluorescent sensor applications is their barrel structure which protects the inner chromophore from aggregation and quenching by oxygen. Fluorescent proteins can be used as molecular indicators, e.g., by cloning them into live cells [86], or by depositing them on a solid substrate which is then brought in contact with an analyte [56]. In this Thesis, fluorescent proteins were covalently attached to the surfaces of optical fibers.

A number of review papers on the protein deposition on different surfaces was pub-

lished [87, 88]. For example, fluorescent proteins can be attached by: microcontact printing method to various surfaces [89], non-covalent protein adsorption, covalent bonding via specific sites, using various biologically mediated immobilization methods [56], and LB method [90]. The substrates which can be used to deposit proteins are gold and Ta_2O_5[91], bare and silanized glass, silicon, polystyrene, polymethylmethacrylate and others [56]. In this Thesis, Citrine – modification of YFP – was covalently bonded via a cross-linker to optical fibers using SAM technique. Examples of sensor applications of the optical fibers modified with fluorescent proteins are medium pH detection [92] and monitoring of important divalent cations (Ca^{2+}) [86]. Besides, it was shown that fluorescent proteins are sensitive to the activity of various proteases [93].

2.4 Sensor applications of photoactive compounds

There are numerous kinds of chemical and biological optical sensors existing nowadays, thorough reviews of which can be found elsewhere [94, 95]. The field of optical sensors has been a growing research area over the last decades. Sensors are typically based on measurements of absorbance, reflectance, and fluorescence emission. Parameters that can be monitored during the studies of the sample fluorescence are intensity, decay time, anisotropy, quenching efficiency, luminescence energy transfer, and so forth. Typically, chemical or biological sensor consists of two basic elements: transduction platform and signal-processing unit. This Thesis is devoted to the development of transduction platform, i.e. optical fibers functionalized with a layer of photoresponsive molecules, which will be further referred to as a sensor unless otherwise stated.

In this Thesis, chemical and biological sensors were realized based on the measurement of fluorescence intensity and lifetime variations. Changes in the fluorescence intensity can be monitored via direct measurements of a studied sample, or indirectly, via changes occurring to layer(s) of photoactive molecules (deposited on an optical fiber) which interact with the analyte under study. The latter method is among the most commonly used nowadays and this field of research suggests a vast number of applications. In this Thesis, molecular layers of porphyrin and Citrine were utilized to track changes in media: i) with different pH values; ii) volatile organic compounds with various concentrations (as an example, diethylamine (DEA) was studied); iii) with Ca^{2+} ions; and iv) different proteases.

2.4.1 Porphyrin films for sensing of pH and volatile organic compounds (VOCs)

Acidity of solution is one of the key solvent parameters used in chemistry and biochemistry. It is expressed by solvent pH value and can be measured using standard electrochemical methods [96]. Since acidity has great effect on properties of molecules and molecular films the responce of molecules to medium pH can also be used for acidity monitoring. For example, photoactive molecules deposited on modified optical fibers can be used to measure pH. In general, the main advantage of this kind of sensors is their size which can be of micro- [97] or even nano-scale [98, 99]. Another advantages of optical fiber sensors are their immunity to electromagnetic interferences and biocompatibility.

When an optical fiber sensor is immersed into an analyte in question, absorption and/or emission spectrum of deposited molecules changes depending on pH of studied analyte. Examples of such compounds are fluorescein derivatives [100], benzo[c]xanthene dyes [101], coumarin [102] and rhodamine derivatives [103], and porphyrins [104, 105]. In this Thesis, pH values were measured using free-base porphyrin SAM films deposited on modified optical fibers. Porphyrins can be used as pH indicators because of its protonation which leads to drastic changes in emission spectra [105].

Measurements of volatile organic compounds (VOCs) are also very important since VOCs can be very dangerous to human health and may have adverse effects on the environment. Different monitoring techniques are used to detect VOCs such as electrical conductivity [106], mass transduction [107], and optical variation in the physical properties of sensing elements [108]. In the latter case, the optical detection of VOCs is based on the changes of physical and spectroscopical properties of molecular films such as refractive index, thickness, absorption and emission spectra, and fluorescence lifetime.

One of the molecules which change their photochemical properties under exposure to VOCs, is porphyrin (especially, its metallated form) [69, 109]. Metallated forms of porphyrin may form coordination complexes with other molecules (such as alcohols, amines, ethers, and thiols) that has direct effect on absorption and/or emission spectra of porphyrins. Different metals have various coordination abilities [69]. Besides, since porphyrin possesses an extended π-conjugated macrocycle causing different types of intermolecular interactions, the porphyrin aggregates can also be used for the monitoring some VOCs. When exposed to VOCs, the change in the aggregation state, and thus in π-π interactions, may lead to additional modifications of absorption and emission

spectra, which therefore, can be exploited in sensor applications [68, 71]. In this Thesis, changes in fluorescence intensity and lifetime of Zn-porphyrin were utilized to detect DEA concentrations down to a few mM.

2.4.2 Modified YFP films for sensing of pH, Ca^{2+} ions and different proteases

Mutagenesis and protein engineering of GFP, isolated from *Aequorea victoria* (bioluminescent jellyfish) and other organisms (from corals), has resulted in the development of a variety of visible fluorescent proteins with emission spectra maxima ranging from blue to red [85]. These fluorescent protein variants can be further modified to improve its stability and introduce sensitivity to some analytes. The modifications are done genetically by changing the aminoacid sequences in the structure of protein close to the vicinity of chromophore that leads to the conformational changes of the chromophore. These changes influence the fluorescence properties of proteins. Modified proteins can be utilized in chemical and biological sensing applications [110, 111]. In this Thesis, Citrine that is modified yellow fluorescent protein (YFP), was used. Citrine is known for its stability to environmental conditions, its higher resistance to photobleaching, high quantum yield of fluorescence and relatively long fluorescence lifetime [110, 112].

Emission spectrum of Citrine in solution is known to be sensitive to the variations of pH in the range 4 – 7 [110], which is due to the protonation of the inner chromophore and conformational structural changes which occur close to the chromophore at low pH [92, 113]. In this Thesis, Citrine was used to monitor changes in pH values of different buffer solutions.

Another important element which can influence emission properties of modified proteins is calcium ion. Ca^{2+} is one of the most important divalent cations present in the biological cell, as well as in many body fluids. Calcium is an integral component of body muscles, nervous system, bones, teeth, and it helps to produce enzymes and hormones necessary for releasing energy in human body. Moreover, calcium plays a crucial role in maintaining body metabolism and digestion. The effects of calcium ions on fluorescence of different proteins were thoroughly studied previously [86, 114]. Applications of fluorescent protein to monitor intracellular Ca^{2+} levels (down to μM concentrations) are widely exploited [86, 115]. Particularly, Citrine was applied to monitor utterly low Ca ions concentrations by Griesbeck and co-workers [110]. In this Thesis, Citrine was used to detect μM concentrations of Ca^{2+} in buffer solutions.

Apart from pH, one of the factors which limits the use of fluorescent proteins in sensor applications is their sensitivity to proteases. Proteases are known for their ability to start catabolism which leads to the destruction of peptide bonds linking amino-acids in proteins (so-called proteolysis) and thus, causing the collapse of protein structure. One of the example of such kind of proteins which undergo proteolysis is those of globular class. On the other hand, β-barrel proteins (to which Citrine belongs) are known to be highly stable to proteolysis in solutions [93]. In this Thesis, Citrine deposited on EOF surfaces, was tested for the changes in fluorescence spectrum when being exposed to various proteases, such as trypsin, chymotrypsin, papain, and pepsin.

A thorough review of different immobilization techniques on various types of surfaces and their applications to chemical and biological sensing, can be found elsewhere [56]. However, to the best of our knowledge, there were no publications on Citrine site-specific covalent immobilization on EOF surfaces and its utilization in sensing of pH, Ca ions, and activity of various proteases.

3 Materials and Methods

3.1 Monolayer deposition methods

3.1.1 Langmuir-Blodgett (LB) method

5,10,15,20-Tetrakis(pentafluorophenyl)porphyrin (PFP) was synthesized in Laboratory of Chemistry, Tampere University of Technology, using the standard procedure of monopyrrole condensation as described elsewhere [116]. Octadecylamine (ODA) (purity 97 %, Sigma), chloroform (purity $\geq 99.8\,\%$, HPLC grade, J.T. Baker), hexane (purity $\geq 99\,\%$, HPLC grade, Lab-Scan) and chromic sulfuric acid ($H_2SO_4 \geq 92\,\%$, $CrO_3 \geq 1.3\,\%$, Merck) were used as supplied. Buffer was prepared with water purified with a Milli-Q© system (Millipore).

Standard multimode step-index fiber AFS 105/125Y (Thorlabs) with a core diameter of 105 μm, a cladding diameter of 125 μm, and a NA of 0.22 was used to prepare TOFs for LB deposition. The length of the TOFs waist and transition regions were 20 and 15 mm, respectively. Glass plates (Menzel-Gläser) with sizes $50 \times 12 \times 1$ mm and $32 \times 12 \times 1$ mm were used as substrates for reference samples. The detailed pre-cleaning and LB deposition procedures can be found elsewhere [**I**]. All PFP/ODA films were deposited with PFP concentrations of 10 mol-%. LB deposition of PFP was carried out with a KSV 5000 instrument. The phosphate buffer containing 1 mM Na_2HPO_4 and 0.2 mM NaH_2PO_4 (pH 6.5) was used as subphase for Langmuir films. A mixture of PFP in chloroform, ODA in chloroform and hexane was spread over the subphase, forming a film of PFP with required concentration in the ODA matrix. The immersion depth of TOFs and reference glass samples varied between 20 and 44 mm in different experiments. The films were deposited at a surface pressure $\pi = 25$ mN/m.

3.1.2 Self-Assembled Monolayer (SAM) method

Porphyrins were synthesized in Laboratory of Chemistry, Tampere University of Technology, using previously described procedure [79]. Isopropylamine (purity $\geq 97\,\%$, GC

(a) (b)

Figure 3.1: The cross-sectional images of (a) HCPBGF [117] and (b) SCPCF used to deposit monolayers of porphyrin.

grade) was purchased from Fluka and 3-aminopropyltrimethoxysilane (APTMS, purity 97 %) was obtained from Aldrich; both were used as supplied. Chloroform (purity $\geq$ 99 %, GC grade, Sigma-Aldrich), dichloromethane (purity $\geq$ 99.8 %, HPLC grade, Sigma-Aldrich), acetone (purity $\geq$ 99.8 %, HPLC grade, Sigma-Aldrich), chromic sulfuric acid (H_2SO_4 $\geq$ 92 %, $CrO_3 \geq$ 1.3 %, Merck), diethylamine (purity $\geq$ 99.5 %, Sigma-Aldrich), hydrochloric acid (VWR), and sulfosuccinimidyl 4-[N-maleimidomethyl]cyclohexane-1-carboxylate (sulfo-SMCC) (ProteoChem) were used as supplied. The coupling buffer (pH 7.2) for protein studies was prepared from 0.1 M sodium phosphate buffer and 5 mM ethylenediaminetetraacetic acid (EDTA). Toluene (purity $\geq$ 99.8 %, HPLC grade, VWR) was distilled over sodium prior to use. Water was purified with a Milli-Q© system (Millipore).

Standard multimode step-index fibers AFS 105/125Y (Thorlabs) and WF 105/125 AN (Ceramoptec) with a core diameter of 105 μm, cladding diameter of 125 μm and a NA of 0.22 were used to manufacture TOFs for porphyrin deposition. Standard multimode step-index fiber UV 100/110 P (Ceramoptec) with core diameter of 100 μm, cladding diameter of 110 μm and a NA of 0.22 was used to prepare EOFs for protein attachment. HCPBGF HC19-1550-01 from Blazephotonics (Figure 3.1a) which has a core diameter 20 μm and pitch 3.9 μm was used. SCPCF was experimental fiber from Fiber Optics Research Center of Russian Academy of Sciences, Russia (Figure 3.1b). SCPCF has 30 μm solid central core and twelve 25 μm holes.

The procedure of the SAM deposition of porphyrins was the same for TOFs and PCFs. During porphyrin deposition on TOFs, glass plates $25 \times 12 \times 1$ mm from Menzel-Gläser were used as substrates for reference samples. Before the SAM procedure, TOFs and reference glass samples were cleaned by successive immersion in dichloromethane,

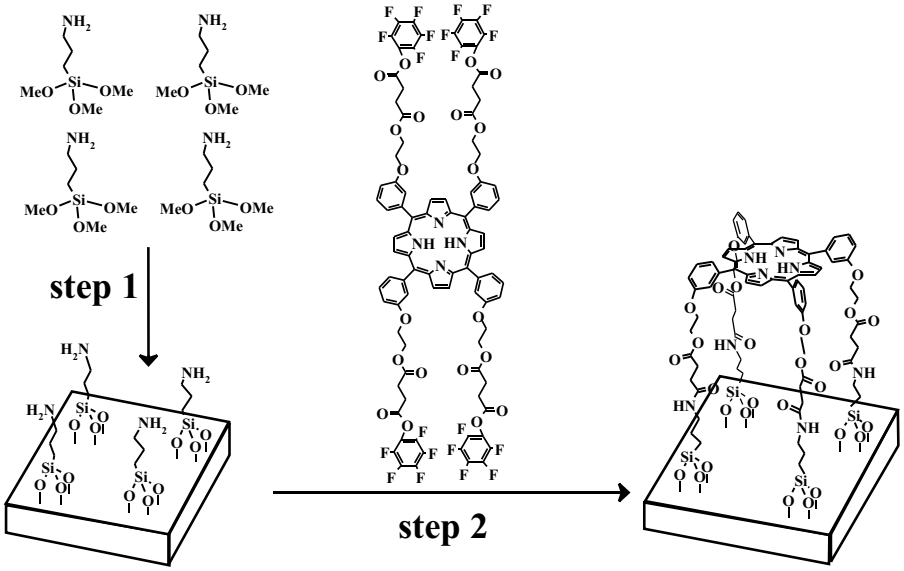

Figure 3.2: The structures of compounds together with the two reaction steps used to functionalize TOFs, PCFs, and reference glass plates by the SAM porphyrin layer [**III**].

acetone and water in an ultrasonic bath for 15, 2 and 5 minutes, respectively. They were further treated with chromic sulfuric acid in ultrasonic bath for 15 min and then rinsed with flowing water for 10 minutes. Then TOFs together with the reference glass plates were fixed in the reaction cell.

Porphyrin attachment to TOFs and glass samples was achieved in two successive steps as presented in Figure 3.2. The more detailed description of the SAM procedure can be found elsewhere [**III**]. Shortly, the first step is the surface activation by APTMS, and the second is the amidation reaction resulting in the formation of the porphyrin film. During the first step, the solution of APTMS (210 μL) and isopropylamine (420 μL) in dry toluene (20 mL) is injected into the reaction cell with TOFs and glass plates (100 °C for 1 hour unless otherwise stated). During the second step, a solution of 70 μM porphyrin in dry toluene was injected into the cell heated to 100 °C for 1 hour unless otherwise stated.

A pressure cell (PC) was used to pump the required solutions through PCF. The PC with installed fibers was kept under an absolute pressure of 6 bar of pure nitrogen. In order to heat a fiber during the deposition procedure, a part of it was placed into a glass vial filled with glycerol heated to100 °C. Before the SAM procedure, chloroform, acetone, water, 1 mM NaOH, and then water were successively injected into PC and pumped through the fibers for 30 minutes each. After that PC was dried in the heated

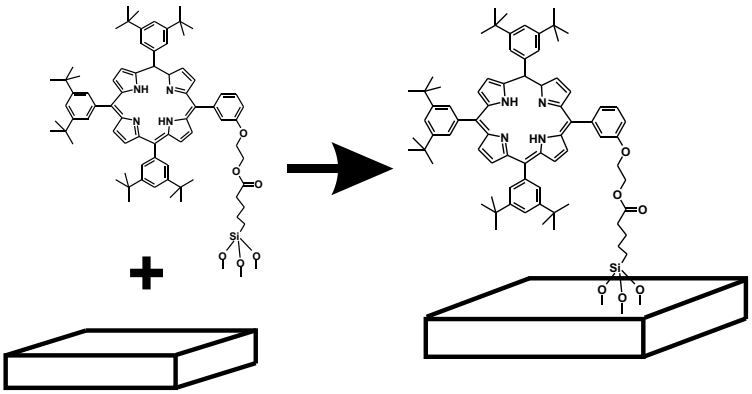

Figure 3.3: The structures of compounds together with the reaction step used to functionalize SCPCFs and reference glass plates with the SAM porphyrin layer.

vacuum chamber (125 °C) for 2 hours.

Another procedure which can be utilized to deposit SAMs of porphyrins on glass surfaces is shown in Figure 3.3. It was thoroughly described in [118]. In this case, mono(triethoxysilane) porphyrin (MTESP) was deposited on the walls of the channels of solid-core photonic crystal fibers (SCPCFs). MTESP was prepared from the corresponding hydroxy-porphyrin by (i) acylation with 4-pentenoic acid under DCC/DMAP conditions, and (ii) hydrosylilation of the terminal double bond with triethoxysilane catalyzed by Karstedt catalyst (Platinum(0)-1,3-divinyl-1,1,3,3-tetramethyldisiloxane complex). Optical fibers were pre-cleaned before the SAM procedure. Chloroform, acetone, water, 1 mM NaOH, and water were successively injected into PC and pumped through the fiber for 30 minutes each. After that, PC was dried under heat in vacuum chamber (125 °C) for 2 hours. The PC with installed fibers was kept under an absolute pressure 3 bar of pure nitrogen. A part of fiber was heated by placing it into a glass vial filled with glycerol at 100 °C. The solution of MTESP (2 mg) and isopropylamine (400 μL) in dry toluene (20 mL) was injected into the PC with installed fibers and pumped through SCPCF by nitrogen pressure for 2 hours. After that, the fiber was washed with toluene, toluene/acetone 1:1 and dichloromethane for 10 minutes, each step. Finally, the PC was purged with nitrogen for 15 minutes.

The self-assembling scheme of porphyrins on PCFs was similar to that on TOFs as shown in Figure 3.2. The more detailed description can be found elsewhere [**IV**]. The solution of APTMS (100 μL) and isopropylamine (200 μL) in dry toluene (10 mL) was injected into the PC which was flushed with nitrogen for 1 hour. During the second step, solution of 426 μM porphyrin in dry toluene was injected into the PC and it was pumped

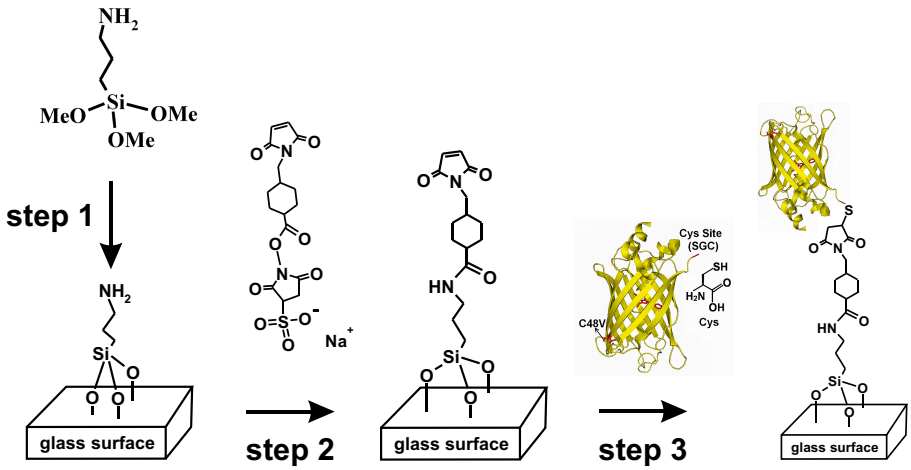

Figure 3.4: The structures of compounds together with three reaction steps used to functionalize EOFs and reference glass plates by YFP SAM [**V**].

for 1 hour. PC was further purged with toluene and dichloromethane for 10 minutes to remove all unreacted compounds.

The protein SAMs were deposited on EOFs and reference glass plates. The cleaning procedure for the substrates is described in more details elsewhere [**V**]. YFP self-assembling on EOFs and glass plates was achieved in three successive steps as presented in Figure 3.4. The first step is the surface activation by APTMS that is similar to that described previously for STOFs [**III**]. The second step is the maleimide-activation of the amino-modified surface with cross-linker sulfo-SMCC, and the last step is the cross-link of modified YFP to the activated surface. A more detailed description of the two last steps can be found in [**V**]. During the second step, amino-activated samples were immersed into the solution of sulfo-SMCC crosslinker (8 mg) in the coupling buffer (4 mL) for 1 hour at room temperature. The maleimide-activated surface was incubated in the purified YFP ($40 - 50\ \mu$M) at room temperature for 4 hours. The unbound proteins were removed by washing the surfaces with the coupling buffer. The surfaces with protein SAMs were stored in the same buffer with 0.02 % sodium azide at 4 °C for further usage.

3.2 Tapering and etching procedures. Measurements of fiber profiles

Two different tapering workstations were used to prepare TOF samples. For LB film deposition, tapered fibers were manufactured following the method proposed by Rusu

and co-workers [20]. Shortly, the fiber was heated by two hydrogen-oxygen burners equipped with separate gas flow controllers. The fiber throughput during tapering was monitored by launching the monitoring light at 532 nm into the fiber input and reading the transmitted power continuously. The tapering rig was fully computer controlled. A double-stage tapering strategy was applied. First, the fiber was pulled under a fixed heated zone until the waist diameter reached the required value. Then the heated zone size increased linearly with progressive pulling of the fiber until the target waist diameter and length were reached. With this procedure, long-tapered optical fibers (LoTOFs) having waist length 20 mm and transition region length 15 mm, were manufactured.

For SAM deposition of porphyrins, another tapering workstation consisted of two translation stages equipped with fiber clamps and a ceramic heater was utilized [**III**]. The tapering rig was computer controlled as well. The procedure was divided into two phases - a preheat phase and a tapering phase. During the preheat phase, the ceramic heater temperature increased from 1200 °C to 1450 °C during 50 s without activating the translating stages. In the tapering phase, the stages pulled the preheated fiber in opposite directions with a speed of 20 μm/s for 130 s and 40 μm/s for 230 s. The temperature of the heater during the tapering phase was kept at 1450 °C. With this procedure, short-tapered optical fibers (STOFs) having waist length shorter than 10 mm and transition region length 25 mm, were produced.

In order to prepare EOF samples, standard chemical etching procedure was employed [28]. Sulfuric acid (95 %, VWR) and 40 % water solution of hydrofluoric acid (technical grade, Merck) were used as supplied. The polyimide buffer of the fiber was removed with 95 % water solution of sulfuric acid under 150 °C. Then, fibers were immersed into 40 % water solution of hydrofluoric acid for 23 minutes, thus giving the etched core diameter of around 70 μm.

After the pulling and etching procedures, diameters and transition slopes of TOFs and EOFs were examined using a WYKO NT1000 surface profiler (Veeco Instruments Inc.) in vertical scanning interferometry (VSI) mode with an optical resolution 2.5 μm in lateral direction. Automated image analysis software was used to measure the taper characteristics over the entire length.

3.3 Steady-state spectroscopy of glass plates and optical fibers

The absorption and emission spectra of the reference glass samples were acquired by a Shimadzu UV-3600 spectrophotometer and Fluorolog 3 (Spex, ISA) fluorimeter, respectively.

The absorption spectra of modified fibers covered with the films of photoactive molecules were measured using a setup shown in Figure 3.5a (marked as "Absorbance measurements"). A tungsten halogen lamp AvaLight-HAL (Avantes) having an output optical power of 700 μW was used as a light source. The output beam was focused into a 200 μm optical fiber to deliver the light to the samples under study. The signals transmitted by modified fibers were detected using a 200 μm optical fiber connected to a spectrometer (AvaSpec–2048, Avantes). The spectrometer spectral resolution was 2.1 nm. The spectra of transmitted light were recorded before and after molecular film deposition, and further processed to determine the absorbance according to the Beer-Lambert law:

$$A = -\log_{10}\left(\frac{I}{I_0}\right) \tag{3.1}$$

where I_0 is the reference fiber signal, i.e. the transmitted light intensity before the film deposition, and I is the transmitted light signal after the deposition.

The emission spectra studies of modified fibers were carried out either with the setup shown in Figure 3.5a (marked as "Emission measurements") or with the layout presented in Figure 3.5b. Two diode lasers, LDH-P-C-405B (PicoQuant) and LDH-P-C-485 (PicoQuant) emitting at 405 and 483 nm, respectively, were used for excitation. The excitation repetition rate was 40 MHz and the power at the input facet of fiber under study was 750 and 50 μW at 405 and 483 nm, respectively. The laser beam was collimated by a telescope condenser, TC (F240APC-A, Thorlabs), giving the beam diameter around 3 mm at the surface of dichroic mirror, DM (NT47-267, Edmund Optics). The DM reflected light in the blue spectral region while transmitting the beam in the spectral region above 520 nm. The reflected laser beam was focused with the lens, L (LB1811, f = 35 mm, Thorlabs) onto the facet of the fiber under study. The same fiber facet was used to collect emission from the layer of photoactive molecules. After passing through the DM, fluorescence was focused onto the facet of the 200 μm optical fiber connected to AvaSpec–2048 spectrometer.

(a)

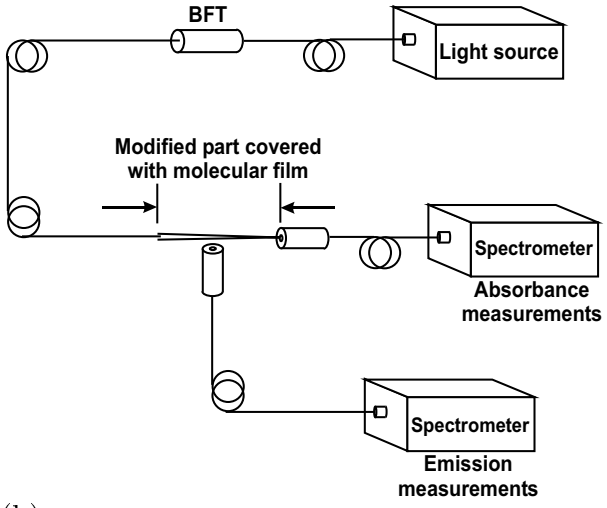

(b)

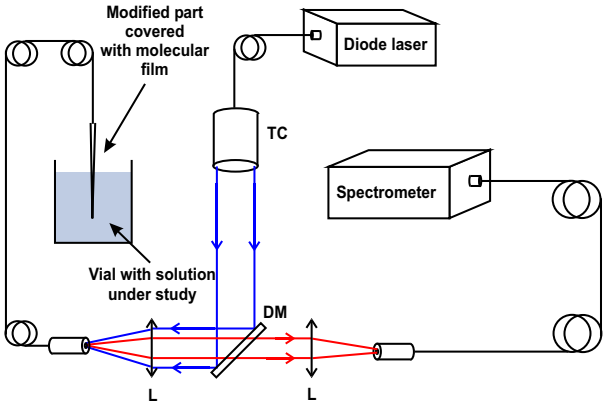

Figure 3.5: The schemes of experimental setups used to measure (a) absorption spectra (Absorbance measurements) and emission spectra along the tapered part of modified fibers (Emission measurements), and (b) emission spectra in sensor applications. BFT – bare fiber terminator, TC – telescope condenser, DM – dichroic mirror, L – lens.

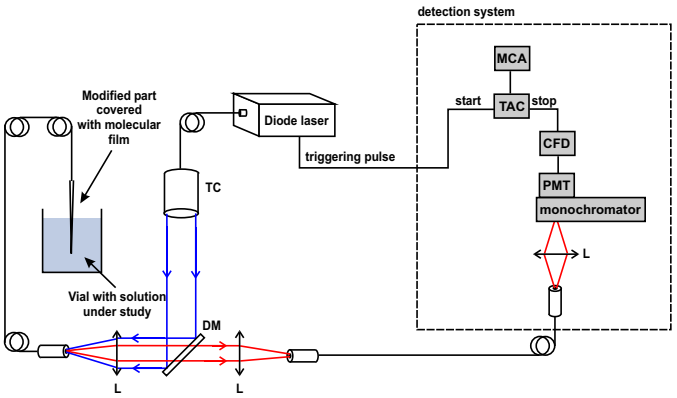

Figure 3.6: Scheme of time-correlated single photon counting (TCSPC) method. TC – telescopic condenser, L – lens, DM – dichroic mirror, PMT – photomultiplier tube, CFD – constant fraction discriminator, TAC – time-to-amplitude converter, and MCA – multichannel analyzer.

3.4 Time-resolved measurements

3.4.1 Time-correlated single photon counting (TCSPC)

Fluorescence decays of the samples in the nanosecond time scale were measured using a time-correlated single photon counting (TCSPC) method (Figure 3.6) [119]. The samples were excited by the laser pulses. The emission of samples was collected with the same experimental setup shown previously in Figure 3.5b. The fluorescence of photoactive molecules is focused with the lens and passed to a photomultiplier tube (PMT) coupled with a monochromator. PMT works in photon counting mode, which means that each detected photon generates an electric pulse on the photomultiplier output.

The electric pulses from PMT are directed to the constant fraction discriminator (CFD). CFD uses a constant fraction of the input pulse to generate square output pulse. The triggering pulse (or so-called start pulse) from the diode laser and signal from CFD (or so-called stop pulse) are passed to the time-to-amplitude converter (TAC), which is the pulse controlled generator of linearly rising voltage. After the start pulse, the TAC output voltage increases linearly with time until the emission photon pulse from CFD stops the TAC generator. The output voltage of the TAC is proportional to the delay between the excitation pulse and the first photon detected by PMT, and it is analyzed by the multichannel analyzer (MCA). Each channel of MCA is associated with some voltage interval and hence, with some delay time interval. After repeating excitation sufficiently many times the MCA channels store information on number of photons detected at different delay time after excitation, which is emission time profile of the sample in

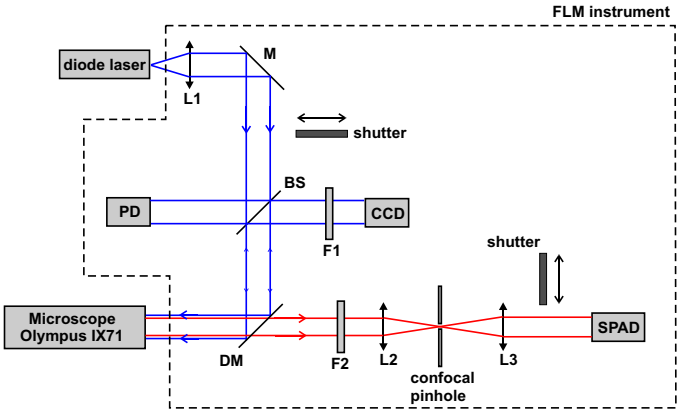

Figure 3.7: Simplified scheme of the fluorescence lifetime microscopy (FLM) instrument. L – lens, M – mirror, F – filter, BS – beamsplitter, DM – dichroic mirror, PD – photodetector, CCD – charge-coupled device, SPAD – single-photon avalanche diode.

response to the pulsed excitation.

The excitation wavelength in TCSPC studies was 405 nm, and the time resolution was approximately 60 – 70 ps (FWHM of the instrument response function).

3.4.2 Fluorescence lifetime microscopy (FLM)

Fluorescence lifetime microscopy (FLM) is generally an imaging technique for producing an image based on the differences in decay rate of the emission from a fluorescent sample. In this Thesis, the FLM images were obtained with the time-resolved fluorescence microscopy instrument MicroTime-200 (PicoQuant GmBH, Berlin, Germany) coupled to the inverted microscope Olympus IX71 (Olympus, Japan) (see Figure 3.7 for details). This instrument uses a confocal light detection setup and the method of TCSPC for data acquisition.

Studied fibers and reference glass plates (pre-installed into Olympus IX71 holder) are illuminated with the diode laser. The laser beam is firstly collimated with lens L1 and then, about 15 % of it is reflected by the beamsplitter (BS) to the photodiode (PD) which is used to control the input laser power. The laser beam which passed through BS, is then reflected by the dichroic mirror (DM) and passed to the microscope Olympus IX71. The microscope objective focuses the excitation beam into single spot at the sample. The same objective collects the sample emission, which is passed back to DM. The sample holder is mounted on a special XY-scanner which allows to scan the sample and obtain an image. Charge-coupled device (CCD) is utilized to monitor

the backscattered excitation light. CCD makes it possible to optimize the position and

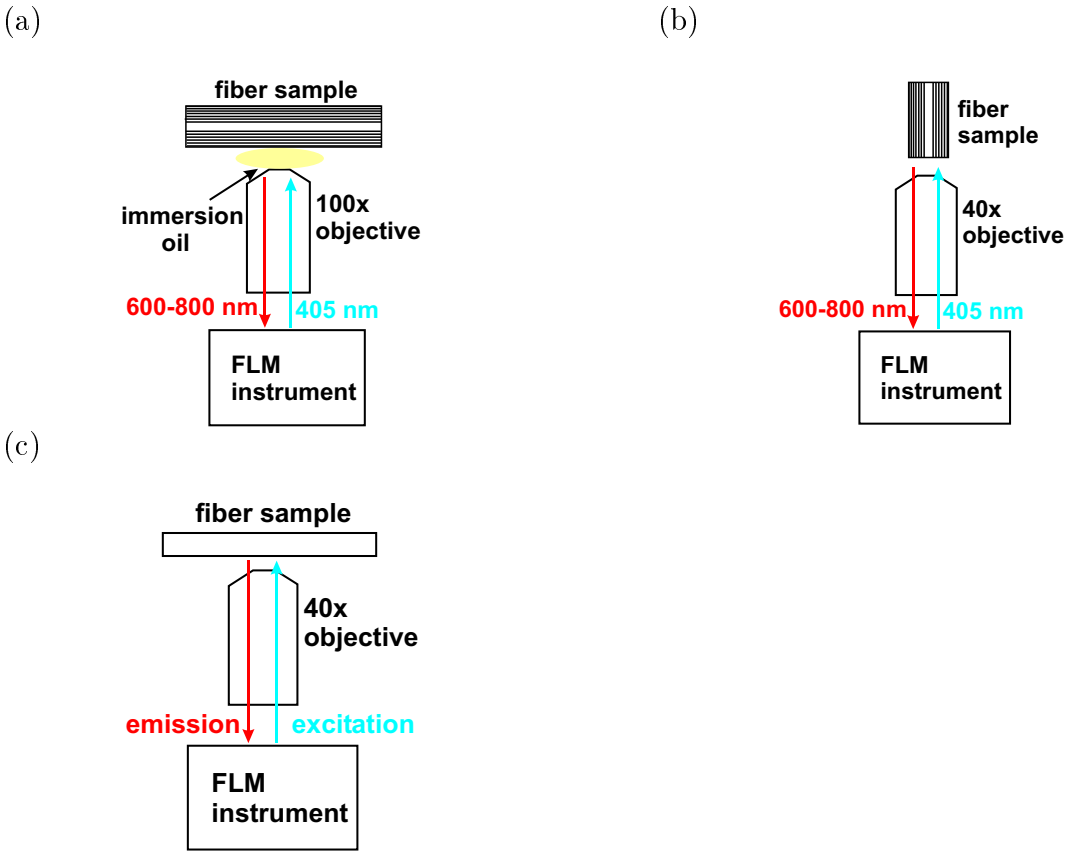

Figure 3.8: Schemes used to obtain: (a) FLM images along PCFs, (b) cross-sectional FLM images of PCFs with attached porphyrins [**IV**], and (c) FLM images of TOFs, EOFs, and reference glass plates with attached porphyrins and proteins.

quality of the excitation light focus.

The fluorescence from the studied samples is collected by the Olympus IX71 optics and passed through DM and a filter F2 to select photons in the wavelength range of interest. Furthermore, two lenses, L1 and L2, and a pinhole are used for the spatial filtration of the signal, i.e. to reject photons emitted not from the focus spot of the microscope objective. Finally, the sample emission is passed to the single-photon avalanche diode (SPAD) which works in the single-photon counting regime. Two shutters are installed in the excitation beam path and in front of the SPAD to ensure safe operation of the system. The obtained FLM images give information about the intensity (brightness) and average lifetime (color) of the samples in question.

Two diode lasers from PicoQuant GmBH were utilized to carry out FLM studies presented in this Thesis, LDH-P-C-405B and LDH-P-C-485 emitting at 405 and 483 nm, re-

spectively. The latter was used to excite samples with attached proteins. DMs Z405RDC (reflectivity R > 90 % for wavelengths below 405 nm; transmission T > 85 % for wavelengths 430 – 800 nm) and Z500DCXR (R > 90 % for wavelength range between 405 and 491 nm; T > 90 % for wavelengths 507 – 700 nm) were utilized to study samples with deposited porphyrins and proteins, respectively. Both DMs are from AHF Analysetechnik, Germany. Filters F2 HQ430LP (T > 90 % for wavelengths higher than 467 nm) and HQ510LP (T > 90 % for wavelengths higher than 520 nm) were used to obtain fluorescence signals from samples with deposited porphyrins and proteins, respectively. Both filters are from Chroma Technology Corp., USA. Microscope objective 100× (with spatial resolution 0.3 μm) applied with the immersion oil, was used to study the fluorescence from PCFs. All other measurements were carried out with 40× objective (0.5 μm spatial resolution). The maximum scan area was 80×80 μm^{2}and the time resolution was 60 – 70 ps. The manufacture software was used to calculate the lifetime map images.

Three different detection schemes were used to study functionalized fibers and glass plates, as shown in Figure 3.8. The 100× objective (with a NA 0.8) with the immersion oil was used to study the distributions of fluorescence lifetime and intensities along modified PCFs (Figure 3.8a). The immersion oil between the objective and sample enables to observe fiber cross-section, since the refractive index of the oil matches that of the fiber. With this method molecular layer deposited inside the channels of PCFs were studied. The 40× air-spaced objective with a NA 0.65 was utilized to obtain the cross-sectional FLM images of PCFs with attached porphyrins (Figure 3.8b). It was also used to obtain FLM images of TOFs, EOFs, and reference glass samples modified with porphyrins and proteins (see Figure 3.8c).

4 Results and discussion

4.1 Long-tapered optical fibers (LoTOFs)

4.1.1 Steady-state spectroscopy of LB films

Absorption and emission spectra of 10 mol-% PFP LB films covering LoTOFs were measured [**I**]. Absorbance of LoTOFs is at least 80 times higher than that of reference glass plates as shown in Figure 4.1a. The absorption peak positions are in a good agreement with those reported previously for glass samples [81]. Soret band maxima at 427 nm of the three LoTOF samples and Q band peak at 505 nm of 10 μm LoTOF sample were expected to be higher than those measured in the experiment. The discrepancy is due to the instrumental effects which are low intensity of the monitoring light in the blue spectral region, high absorption of the samples, and reduced sensitivity of the spectrometer in the blue region of the spectrum.

The results of absorption studies are brought together in Table 4.1 [**I**]. The positions of the absorption bands of LoTOF samples are in a good agreement with those obtained for the reference glass plates.

Typical emission spectra of studied TOFs together with the normalized spectrum of 1.8 μM solution of PFP in chloroform are presented in Figure 4.1b. There are three peaks in the emission spectrum of PFP film deposited on the flat glass sample (at 640, 663 and 704 nm), and only two maxima are observed for TOFs, at 650 and 703 nm. The latter resembles the emission spectrum in solution which also has two maxima, but at slightly different wavelengths, 639 and 707 nm. The emission spectrum of the film on a flat surface of the glass plate has a shape with three peaks as reported previously [81], while the spectra of films on tapered fibers have two peaks that is typical for disordered aggregates of tetraarylporphyrins in LB films [120]. It is clear from Figure 4.1b that PFP in ODA matrix shows different aggregation properties depending on whether it has been deposited on a glass plane or on an optical waveguide with a curved surface.

Emission spectra measurements were used to optimize geometry of conical part of

(a) (b)

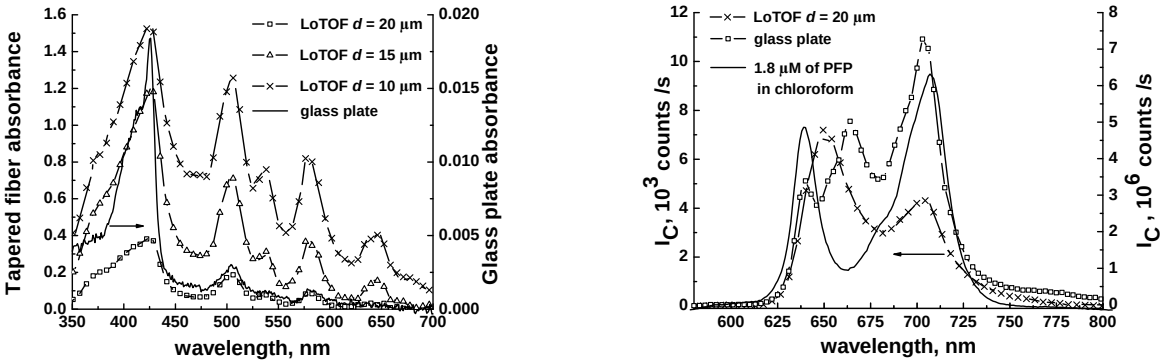

Figure 4.1: (a) Absorption spectra of long tapered optical fibers (LoTOFs) (left Y-axis) having different tip diameters, d, and reference glass plate (right Y-axis). (b) Corrected emission spectra of 1.8 μM solution of PFP in chloroform (right Y-axis, excitation wavelength is 411 nm), and 10 mol-% PFP in ODA matrix monolayer on a glass sample (right Y-axis, excitation wavelength is 427 nm), and 10 mol-% PFP in ODA matrix filmed on LoTOF with tip diameter d = 20 μm, measured at a distance 21.5 mm from tip end (left Y-axis, excitation wavelength is 404 nm) [**I**].

Table 4.1: Absorbance of different LoTOFs and reference glass sample covered with monolayer of 10-mol% of PFP in ODA [**I**]. Positions of the bands, λ_{max}, are given in nm.

Sample	Soret band		Q-bands							
	λ_{max}	A	λ_{max}	A	λ_{max}	A	λ_{max}	A	λ_{max}	A
1.8 μM of PFP in chloroform	413	0.588	506	0.041	–	–	584	0.014	–	–
Glass plate	426	0.018	504	0.003	537	0.001	578	0.001	–	–
LoTOF $d = 20$ μm	425	0.397	504	0.193	538	0.077	580	0.078	644	0.029
LoTOF $d = 15$ μm	426	1.224	504	0.729	537	0.316	578	0.389	646	0.146
LoTOF $d = 10$ μm	424	1.549	505	1.264	538	0.758	578	0.833	644	0.398

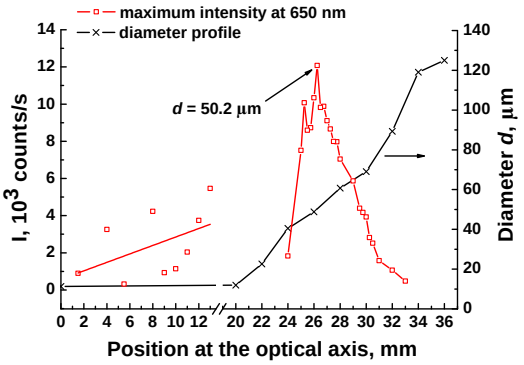

Figure 4.2: Typical distribution of emission intensity taken along LoTOF with tip diameter 10 μm [**II**]. In the region $0-12$ mm the linear fit was used.

tapered fiber employing the scheme shown in Figure 3.5a and marked as "Emission measurements". Distribution of emission intensity along fiber optical axis, taken at PFP fluorescence maximum at 650 nm and presented in Figure 4.2, can be used as indicator of evanescence field at the fiber surface. Based on the presented results, it can be concluded that in order to obtain high enough emission intensity, it is enough to taper and cut TOFs near the transitional region (to produce so-called STOFs) rather than to obtain a long region with small diameter (LoTOFs).

4.1.2 Fluorescence lifetime microscopy (FLM) measurements of LB films

Typical fluorescence lifetime images obtained for PFP layers on flat quartz substrate and TOF are presented in Figure 4.3, which unambiguously shows that PFP aggregates differently on plane and curved surfaces. On a flat glass surface a grained structure of PFP in ODA was typically observed after LB deposition. The characteristic size of the PFP domains in this case was found to be a few micrometers. On the other hand, FLM images of LoTOFs showed uniform PFP/ODA distribution with a minimum FLM spatial resolution of 0.5 μm.

White line rectangles in Figure 4.3 mark regions used to study the fluorescence decay profiles of the samples. Typical fluorescence decay curves of PFP/ODA films on a reference glass plate and on LoTOF are shown in Figure 4.4. A bi-exponential decay fit gave lifetimes $\tau_1 = 417\pm8$ ps (97 %) and $\tau_2 = 2.32\pm0.19$ ns (3 %) resulting in the average weighted emission lifetime of $\tau_{AV} = 0.47 \pm 0.01$ ns for LoTOFs, and $\tau_1 = 2.6 \pm 0.06$ ns (87 %) and $\tau_2 = 5.04 \pm 0.29$ ns (13 %) with average lifetime $\tau_{AV} = 2.92 \pm 0.09$ ns for the

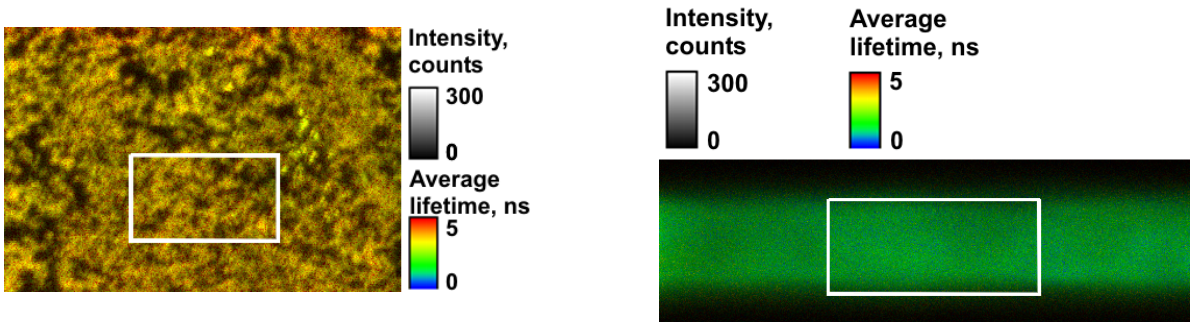

Figure 4.3: Two typical images showing fluorescence intensity and lifetime distributions over glass plate sample (left-hand side image) and LoTOF ($d = 15$ μm, right-hand side image) covered with 10 mol-% PFP/ODA films. FLM image of glass plate sample has size 60×40 μm^2; FLM image of tapered fiber sample has size 24×80 μm^2. At each point, brightness and color denote intensity and average lifetime of fluorescence, respectively. White rectangles show areas used to obtain fluorescence decay curves.

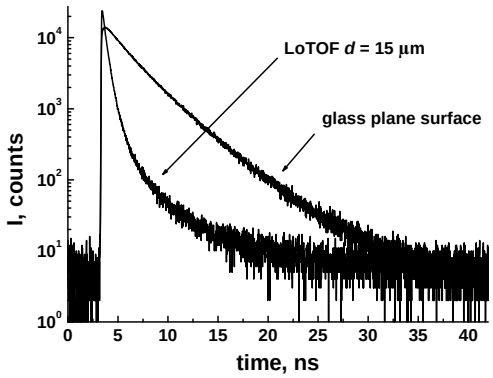

Figure 4.4: Fluorescence decay curves of 10 mol-% PFP/ODA film on glass plate and LoTOF with tip diameter $d = 15$ μm [**I**].

glass plate. The latter values are in a good agreement with results reported previously [81], namely $\tau_1 = 3.0 \pm 0.65$ ns and $\tau_2 = 5.5 \pm 0.35$ ns.

The fluorescence lifetime decay profiles of the PFP/ODA films on LoTOFs are multi-exponential with average weighted fluorescence lifetime of 0.5 ns. These properties are typical for porphyrin aggregates in LB films, and they arise from inter-chromophore interaction, energy transfer and enhanced quenching of the excited state. Contrary to that, the excited state lifetime of the PFP film on the flat surface is almost as long as that of PFP in solution. The proposed explanation for this phenomenon is the formation of J–type aggregates with a low density of defects responsible for excited state quenching. The study presented in this Thesis reveals that surface curvature can be the factor

increasing the number of defects (another phenomenon leading to the increased number of defects is the PFP concentration decrease) and thus reducing the lifetime of the excited state. Emission properties, spectra and lifetimes of the PFP films deposited on LoTOFs are similar to those of many other LB films of tetraarylporphyrins encapsulated in lipid matrices [120, 121].

Another important observation is the different topology of the molecular layers formed on flat (glass plates) and curved (LoTOFs) surfaces. Relatively big domains, of micrometer size, can be seen for films on flat surfaces (see Figure 4.3, left-hand side image). On the other hand, layers covering LoTOFs show an almost homogeneous coverage of the surface (see Figure 4.3, right-hand side image), which indicates that the aggregate sizes are much smaller than the spatial resolution of the FLM instrument used (0.5 μm). Thus, for aggregates of smaller size the lifetime of the excited state is shorter, and their internal organization is probably rather disordered, as is the case with most other porphyrins [120–122].

Since the same Langmuir layer was used to deposit PFP films onto both flat and curved surfaces, but different aggregates were found on the surfaces with different curvatures, the film restructuring must happen at the meniscus. The radius of curvature of the meniscus is much smaller for the fibers than that for the 12 mm wide glass plates. The characteristic size of PFP domains found on a flat surface, $1 - 2$ μm, is comparable with the optical fiber diameter and the size of the meniscus curvature around fibers in the LB trough. The small curvature size most likely forces the micron-sized PFP domains to break into smaller domains with a rather disordered structure and relatively large number of defects (that is also confirmed by the results of studies presented before in Section 4.1.1), thus reducing the lifetime of the singlet excited state.

4.2 Short-tapered optical fibers (STOFs)

4.2.1 Steady-state spectroscopy of porphyrin SAM films

Real-time steady-state absorption studies

Figure 4.5 shows the absorption spectra of the glass plates covered with the SAM layers of porphyrin deposited on both sides. The time of surface activation with APTMS (step 1, Figure 3.2) was varied from 1 to 5 hours, while the time of porphyrin attachment was 18 hours for all samples. It is seen from the figure that there are no essential differences in absorbance between the samples with different activation times, and the average

(a) (b)

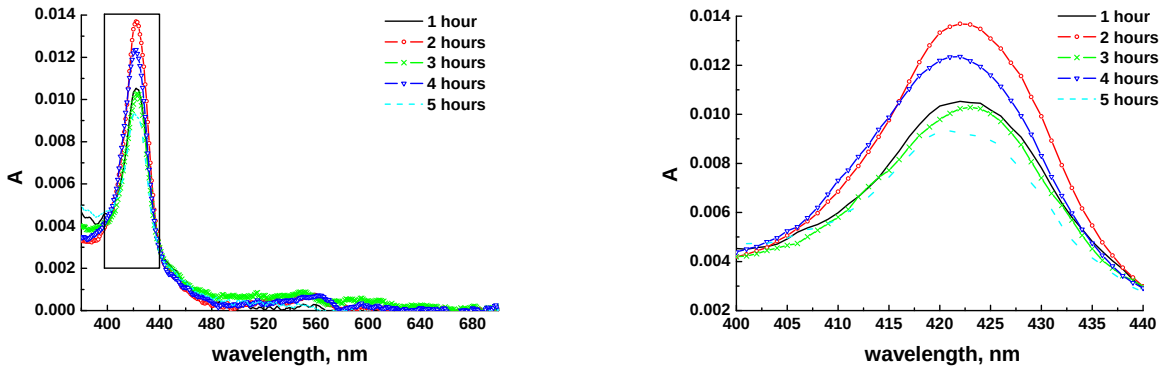

Figure 4.5: (a) The absorption spectra of glass plates covered with porphyrin SAM and (b) its zoomed-in image in the Soret band region. The surface activation time was varied from 1 to 5 hours, and the functionalization time of 18 hours was kept the same for all samples [**III**].

absorbance value obtained at 422 nm is 0.011 ± 0.002 (see Figure 4.5a). Therefore, the activation time of glass samples and STOFs during SAM deposition was chosen to be 1 hour in all further experiments.

To the best of our knowledge, results presented in work [**III**] are novel since previously, there were no measurements of glass surface activation time by APTMS in toluene at high temperature. The activation time varied between 3 and 20 hours in different studies [72, 77, 78] and there were no detailed investigations carried out during the deposition of molecular layers of aminosilanes at 100 °C on glass surfaces. It was previously demonstrated by Kurth and co-authors [123] that using the vapor phase adsorption method the molecular monolayer of APTMS can be deposited in 5 minutes. Since deposition is a diffusion process and it should be slower in a liquid phase, the SAM deposition time of APTMS dissolved in toluene can be expected within 5 – 60 minutes at high temperatures. In another study, silica substrates with deposited acetate-terminated silanes were investigated using atomic force microscopy [124]. The measurements in solutions of dicyclohexyl at room temperature revealed the increase of surface roughness after 1 hour of the deposition procedure, which was attributed to the formation of multilayer structures of deposited molecules. The study presented in this Thesis, shows that the surface activation is completed within 1 hour [**III**].

The formation of the free-base porphyrin SAM on STOF surface (step 2, Figure 3.2) was monitored by recording the absorption spectra during the reaction. The setup used in this study was the same as that shown in Figure 3.5a (marked as 'Absorbance mea-

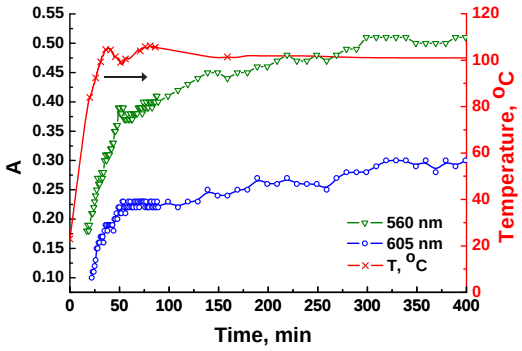

Figure 4.6: The real-time measurements of absorption at 560 and 605 nm during the porphyrin SAM deposition on STOFs. The surface activation time was 60 minutes [**III**].

surements') with the tapered part of the fiber placed into the reactor. The absorbance time profiles at two wavelengths, 560 and 605 nm, corresponding to the maxima of the two absorption bands, are presented in Figure 4.6 together with the reaction temperature plot. At both wavelengths the absorbance doubled during the first 40 minutes when the temperature was increased from 80 to 105 °C. During the following 345 minutes, the absorption values slightly increased from 0.38 to 0.51 and from 0.23 to 0.30 at 560 and 605 nm, respectively.

The presented results are in agreement with other authors who deposited Zn-porphyrins on glass surfaces using the SAM procedure [72]. They demonstrated that after 1 hour, the chemical reaction of porphyrin attachment had already reached its completion. It is clearly seen from Figure 4.6 that the formation of SAM monolayer on the surface of STOF is completed during the first hour of the deposition process. The absorption increases only slightly during following 5 hours, which can be explained by the formation of multilayered porphyrin structures on the STOF surfaces. Indeed, absorbance is proportional to the molecular density on a surface and therefore, rapid increase of A during first 60 minutes means the increase of porphyrin density on STOF surface, whilst slow increase of absorbance during the next 5 hours can indicate that the molecules are somehow imbricated on top of each other.

Steady-state absorption and emission spectra

The absorption spectra of the STOF and the reference glass plate are presented in Figure 4.7a. The absorbance of STOF at 515 nm is about 0.24, which is at least 60 times higher than that measured for the reference glass sample. It is worth mentioning that the

(a) (b)

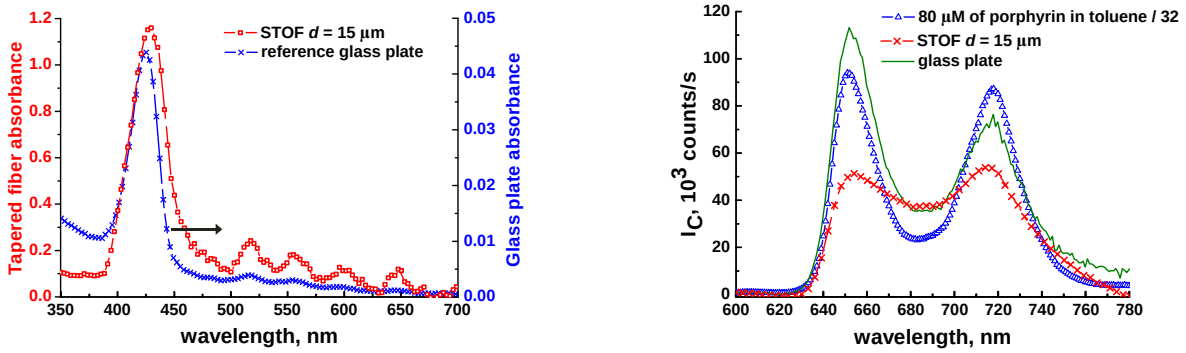

Figure 4.7: (a) Two typical absorption spectra of porphyrin films covalently attached to the surfaces of the reference glass plate and STOF. (b) The corrected emission spectrum of the STOF having tip diameter 15 μm together with those of the reference glass sample and 80 μM solution of porphyrin in toluene [**III**].

Table 4.2: Absorbance of STOFs and reference glass plate covered with free-base porphyrin SAMs [**III**]. Positions of the bands, λ_{max}, are given in nm.

Sample	Soret band		Q-bands							
	λ_{max}	A	λ_{max}	A	λ_{max}	A	λ_{max}	A	λ_{max}	A
Glass plate	431	0.044	515	0.004	553	0.003	597	0.002	648	0.001
STOF $d = 15$ μm	429	1.16	517	0.241	554	0.185	599	0.107	646	0.092

total sensitivity and dynamic range of the spectrometer in the region around 400 nm is lower than in the red part of the spectrum as it was the case for steady-state spectroscopy studies of LB PFP on LoTOFs. Therefore, no absorption comparison can be made between STOFs and reference glass samples at 430 nm. The absorption values of the reference glass plates are in good agreement with the previously reported results of similar porphyrin SAMs on quartz plates [75]. The results of absorption measurements are summarized in Table 4.2. It is evident that Soret and Q-band positions in the absorption spectra of STOFs are in good agreement with those measured for reference glass plates.

The emission measurements of STOFs modified with porphyrin SAMs were carried out using the setup shown in Figure 3.5b. The corrected emission spectra are shown in Figure 4.7b, revealing two peaks at 648 and 718 nm. In order to fit into the plot, corrected emission spectrum of the solution of 80 μM porphyrin in toluene was normalized. The positions of emission maxima are in a good agreement with those measured for the

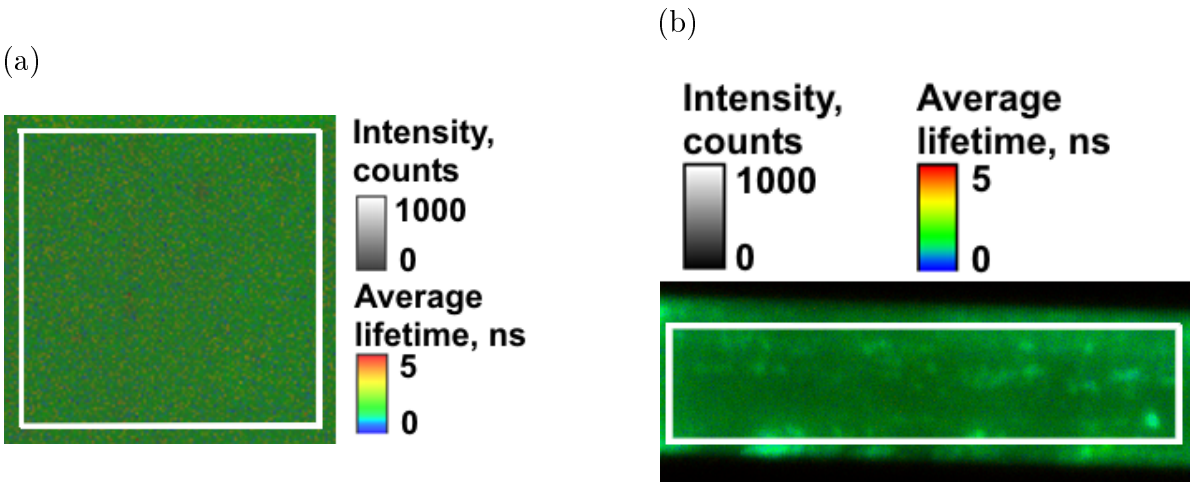

Figure 4.8: Two typical images showing the fluorescence intensity and lifetime distributions of porphyrin SAMs over the reference glass sample (a), and the tapered part of the STOF with $d = 23$ μm (b). Sizes of FLM images are 28×28 μm^2 and 28×74 μm^2 for glass plate and STOF, respectively. At each point, brightness and color denote intensity and average lifetime of molecular fluorescence, respectively. White rectangles show areas used to calculate average fluorescence lifetime.

reference glass sample and solution of 80 μM porphyrin in toluene. Therefore, the spectroscopic properties of porphyrin SAMs are independent of the surface curvature, which was not the case for the LB deposited films on LoTOFs and flat glass substrates [**I**, **II**]. Moreover, the wavelengths of emission maxima match with those at 650 and 710 nm reported previously [75].

4.2.2 Time-resolved measurements of SAM films

In order to study the homogeneity of deposited porphyrin molecules, FLM measurements were carried out [**III**]. The fluorescence lifetime and intensity distributions of porphyrin SAMs on the STOFs and glass plates were obtained using FLM instrument. Two typical images are shown in Figure 4.8. In spite of a few bright spots of micrometer size, the two surfaces are covered homogeneously by the porphyrin SAMs. The areas containing bright spots have slight deviations from the average value of the fluorescence lifetime and presumably they can be ascribed to the polymerization of APTMS taking place at these very spots during the first step of the SAM procedure (step 1, Figure 3.2), and the formation of big porphyrin aggregates at the second step (step 2, Figure 3.2).

The white rectangles in Figure 4.8 show the regions used to calculate accumulative

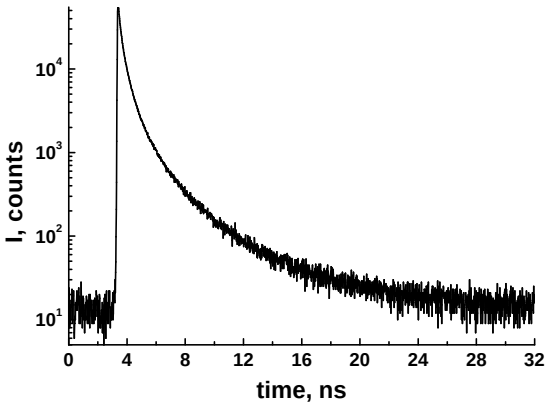

Figure 4.9: A typical fluorescence decay curve of the STOF covered with porphyrin SAM [**III**].

Table 4.3: Average weighted fluorescence lifetimes of free-base porphyrin covering surfaces of STOF and reference glass plate. Pre-exponential amplitudes are given in parentheses [**III**].

Sample	τ_1, ns	τ_2, ns	τ_3, ns	τ_{AV}, ns
Glass plate	0.16 ± 0.01 (75 %)	0.62 ± 0.02 (24 %)	2.79 ± 0.19 (1 %)	0.30 ± 0.01
STOF $d = 15$ μm	0.18 ± 0.01 (73 %)	0.69 ± 0.02 (25 %)	3.01 ± 0.13 (2 %)	0.36 ± 0.01

fluorescence decays, which were further used to evaluate the average weighted emission lifetimes of the samples. A typical fluorescence decay curve for STOF is given in Figure 4.9. Although three exponential decay models were used to fit the fluorescence decays, the individual lifetime has no physical meaning. Therefore, the average weighted fluorescence lifetimes were calculated and summarized in Table 4.3.

The fluorescence lifetimes of SAMs on glass plates and STOFs are in a good agreement with each other with the difference between the two values being less than 17 %. The main contributions to these values are from the short-lived components, which were 0.18 ns (73 %) for the STOF and 0.16 ns (75 %) for the glass sample. The longer-lived components, 0.69 and 0.62 ns, gave 25 % and 24 % contributions to the weighted average fluorescence lifetime value for the STOF and glass plate, respectively, and only less than 2 % of the average fluorescence lifetime value came from the 3.0 ns (STOF) and 2.8 ns (reference glass sample) components. The obtained average lifetime of the free-base porphyrin deposited on the glass surface is six times shorter than that reported for single-bridged free-base porphyrin deposited on top of ITO electrode (1.7 ns) [77]. The short-lived emission can be attributed to more densely packed porphyrin SAMs

reported in this Thesis. Indeed, absorbance obtained in the studies presented in this Thesis (see Figure 4.7a, crosses) is higher than that measured in [77] meaning a more dense package of porphyrins in molecular layers reported here.

4.2.3 Geometry optimization of the coned part of STOFs

Modeling of molecular fluorescence at the coned part of STOF

(a)

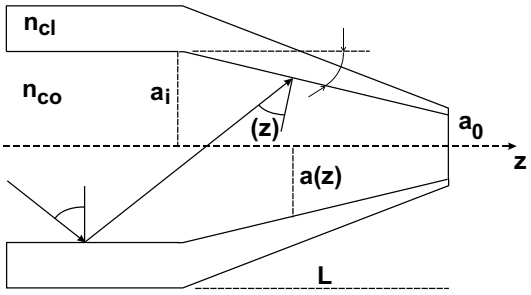

(b)

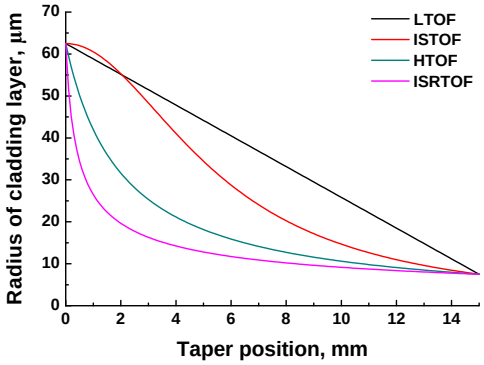

Figure 4.10: (a) Ray path in linearly tapered optical fiber (LTOF). (b) Radius profiles of TOFs of different geometries. For the list of abbreviations used in legend see Table 4.4.

Table 4.4: Radius profiles, $a(z)$, along the fiber optical axis, z, for TOFs of different geometries. $a(z)$ and z are given in μm and mm, respectively.

Equation	A	B	Abbreviation
$a(z) = Az + B$	-3.67	62.5	Linearly tapered optical fiber (LTOF)
$a(z) = \frac{A}{z^2+B}$	1917.61	30.68	Inverse squared tapered optical fiber (ISTOF)
$a(z) = \frac{A}{z+B}$	127.84	2.05	Hyperbolically tapered optical fiber (HTOF)
$a(z) = \frac{A}{\sqrt{z+B}}$	29.26	0.22	Inverse square root tapered optical fiber (ISRTOF)

The propagation of light in TOF can be modeled with ray optics. As it is seen from Figure 4.10a, the angle $\alpha(z)$ between the incident beam and normal to the interface in TOF region depends on the core radius, $a(z)$, as [10]:

$$\alpha(z) = \arccos\left[\frac{a_i \cos\alpha}{a(z)}\right] - \Gamma, \tag{4.1}$$

where Γ is the tapering angle [10]:

$$\Gamma = \arctan\left[\frac{a_i - a_0}{L}\right] \tag{4.2}$$

and a_i and a_0 are radii of the core at the beginning and end of the tapered region. The radii profiles, $a(z)$, along the fiber optical axis are given in Table 4.4 and shown in Figure 4.10b for different geometries of tapered region .

Thus, substituting eqs. (4.1) and (4.2) into eq. (2.4), the dependence of penetration depth d_p on the position z can be expressed as:

$$d_p(z) = \frac{\lambda}{2\pi}\left\{n_{co}^2 \sin^2\left[\arccos\left(\frac{a_i\cos\alpha}{a(z)}\right) - \arctan\left(\frac{a_i - a_0}{L}\right)\right] - n_{cl}^2\right\}^{-1/2} \tag{4.3}$$

Substituting d_p corresponding to different TOF geometries into eq. (2.3), EW intensity distributions can be obtained. Figure 4.11a presents results of calculations carried out for a typical multimode fiber with refractive indices of the core and cladding 1.48 and 1.46 at 430 nm, respectively (AFS 105/125 Y from Thorlabs). As expected, when moving from higher to lower diameter values along TOF, the evanescent field begins to escape first for $\frac{1}{\sqrt{z}}$ profile. For the geometry corresponding to LTOF, the evanescent field begins to escape at the very end of the tapered part of the fiber. In this Thesis, TOFs with profile roughly corresponding to $\frac{1}{z^2}$ function were used.

The changes in the intensity of the guided light, $dI(z)$, when moving along the tapered part of the fiber from higher to lower diameter values, can be expressed as follows:

$$\mathrm{d}I(z) = -\frac{2I(z)}{a(z)} \cdot \left(\frac{a_i}{a(z)}\right)^2 \cdot \left[1 - 10^{-A}\right] \cdot \exp\left(-\frac{2\cdot\delta(z)}{d_p(z)}\right)\mathrm{d}z \tag{4.4}$$

where $I(z)$ is the excitation beam intensity distribution along optical axis z; A is the film absorption coefficient; and $\delta(z)$ is the cladding layer thickness. The cladding layer thickness, $\delta(z)$, was considered to satisfy the following condition in all further calculations:

$$\delta(z) = a(z) \cdot \left(\frac{a_{cl}}{a_i} - 1\right) \tag{4.5}$$

where a_{cl} is the radius of cladding layer in bare, untapered fiber.

(a) (b)

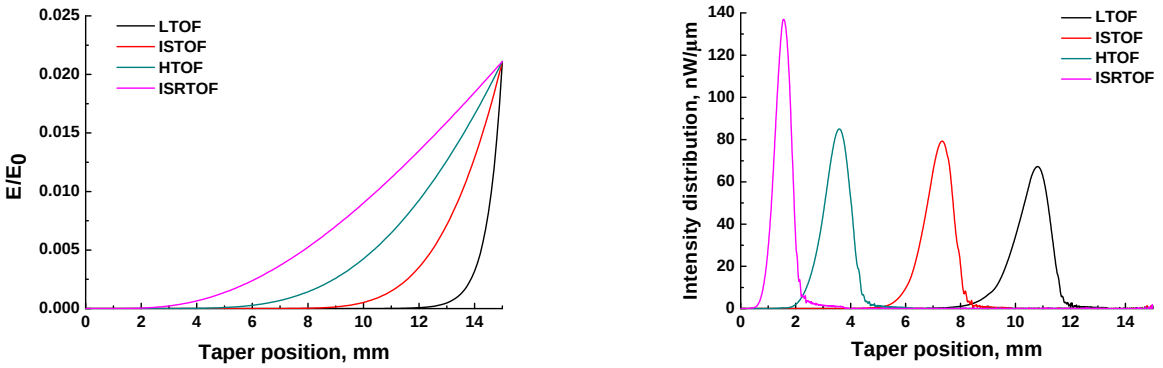

Figure 4.11: (a) Evanescent field distributions along TOF surfaces corresponding to different geometries of tapers. (b) Fluorescence intensity distributions along optical axes of TOFs for different geometries of TOFs. For the list of abbreviations see Table 4.4. Fiber is AFS 105/125Y from Thorlabs, $\alpha = 89°$, $n_{co} = 1.48$, $n_{cl} = 1.46$, laser power at the fiber input 100 μW, and $\lambda = 430$ nm.

Substituting $d_p(z)$ that corresponds to different TOF geometries into eq. (4.4) and solving differential equation (using Matlab software function `ode45`), the distribution of excitation beam intensity along optical axis z of TOF, can be obtained. The fluorescence intensity distribution, $I_{fl}(z)$, is proportional to the variation of excitation beam intensity:

$$I_{fl}(z) \propto -\Delta I(z) \tag{4.6}$$

Thus, the distribution of fluorescence intensity along optical axis z can be determined by solving eq (4.4). The results of calculations are presented in Figure 4.11b for which $\alpha = 89°$, $n_{co} = 1.48$, $n_{cl} = 1.46$, $\lambda = 430$ nm, laser power at the fiber input is 100 μW, and absorption coefficient is 1. As it is clearly seen, the most broad profile corresponds to the linear geometry of TOF, whilst the narrowest region from which molecular fluorescence can be observed has TOF with $\frac{1}{\sqrt{z}}$ profile. Comparing Figures 4.10b and 4.11b it can be noticed that for all TOF profiles, the maximum emission density corresponds to approx. 25 μm radius of TOF, which corresponds to about 4 μm thickness of cladding layer. At this $\delta(z)$, the fiber guided light starts to be absorbed by the molecular layer deposited on its surface and the fluorescence becomes visible at the fiber surface.

(a) (b)

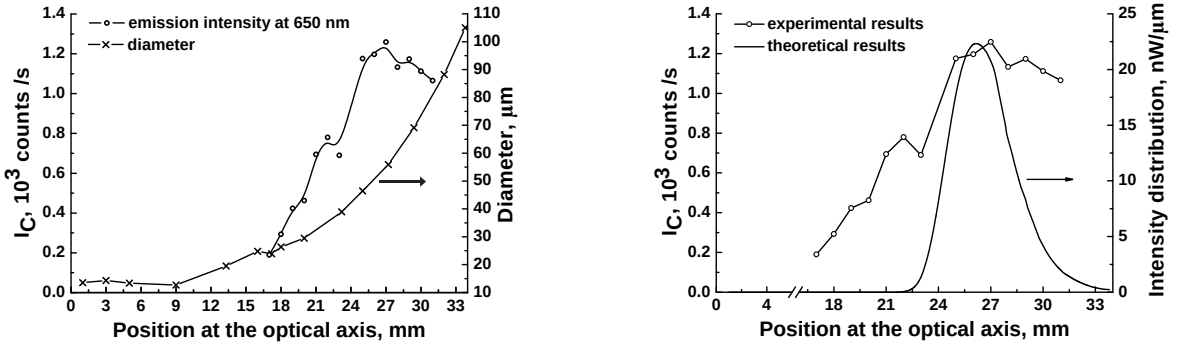

Figure 4.12: (a) Distribution of emission intensity at 650 nm taken along the STOF axis (circles) and diameter profile of the tapered fiber (crosses) [**III**]. (b) Experimental distribution of emission intensity at 650 nm taken along the STOF axis (circles), and emission intensity calculated using eqs. (4.4) and (4.6) (solid line).

Experimental determination of the optimum diameter of STOFs

In order to optimize STOF geometry for sensor applications, two different emission detection schemes were utilized. The first scheme is shown in Figure 3.5a (marked as "Emission measurements", will be further referred to as lateral measurements). It was used to measure the fluorescence intensity of porphyrin SAMs (or equivalently, relative EW intensity) at the surfaces of STOFs along the optical axes of fibers. The spatial resolution was 0.25 mm (determined by the diameter of the core of fiber used for emission collection). The spectrometer sampling intervals were set to integration times between 5 and 10 s. The area on the surface of a STOF, from which emission was collected during one sampling, varied between 0.05 and 0.2 mm^2 for different STOF diameters. The typical distribution of emission intensity at 650 nm along the fiber optical axis together with the STOF diameter profile are shown in Figure 4.12a. The fluorescence intensity distribution clearly shows the region of the EW field maximum between 21 and 29 mm along the fiber optical axis, which corresponds to the coned part diameter between 35 and 82 μm, and the intensity maximum is observed at the fiber diameter of 55 μm.

Figure 4.12b shows results of calculations according to the model discussed above together with experimental data. Theoretical calculations were carried out by solving eqs. (4.4) and (4.6) with $\alpha = 81.7°$, $\lambda = 430$ nm, $n_{co} = 1.48$, $n_{cl} = 1.46$, and the film absorption coefficient 0.02. The position of theoretical curve maximum is in reasonable agreement with that obtained in experiments (the accuracy is limited by the measure-

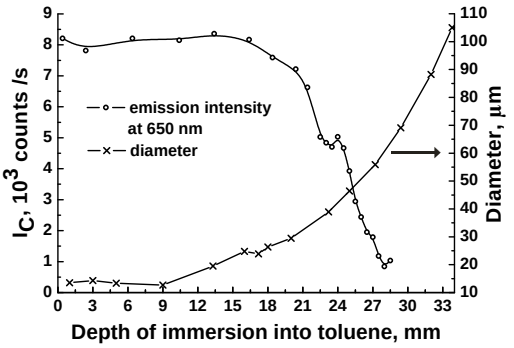

Figure 4.13: The dependence of emission intensity at 650 nm from the STOF on the immersion depth into toluene (circles), and the fiber diameter profile (crosses).

ments of STOF radius profile). As it is seen, the width of theoretical curve is narrower than that of experimental curve. One of the proposed explanations for it is the high value of film absorption coefficient used in the calculations.

In the studies discussed above, the porphyrin emission was gathered from quite a small area of STOF. In order to increase the signal-to-noise ratio of fluorescence signals and to enable the usage of modified STOFs as sensors, the experimental setup presented in Figure 3.5b was utilized. In this case, the fluorescence from porphyrin molecules was collected from the whole coned part of the tapered fiber. During these studies, the coned part was dipped into toluene which has a slightly higher refractive index than that of the cladding layer, thus letting the light to escape from the fiber at the interface between cladding layer and toluene. The depth of immersion was controlled by micrometer screw with an accuracy of 0.01 mm. The results of these measurements together with the diameter profile are summarized in Figure 4.13. There is virtually no change in the emission intensity when immersing the fiber up to the taper diameter of 30 μm, which means that the excitation light does not reach the thinner part of the fiber. At the diameter of 48 μm the emission intensity halves, and almost no emission is observed when the fiber is dipped down to the diameter of 60 μm, i.e. there is no EW field at the surface of the fiber since all the light escapes from the core into the vial with toluene.

The maximum emission intensity was detected at 55 μm diameter of STOF, which corresponds to the cladding layer thickness of 4.4 μm. The incident angle α corresponding to this thickness can be assessed with eq. (2.4), which gives $81.45 \pm 0.02°$ (penetration depth, d_p, is taken to be equal to the cladding layer thickness). According to the optical fiber specifications, the critical angle α_C for the straight part of the fiber is 81.43°. The critical angle $\alpha_C(z)$ for this penetration depth, d_p, calculated using eq. (4.1) with $\cos\alpha_C$

substituted for $\cos\alpha$, is $70.1 \pm 1.2°$. Therefore, the calculated critical angle $\alpha_C(z)$ which corresponds to the diameter of the coned part 55 μm is smaller than the incident angle of the reflected beam of 81.45°, for which the penetration depth d_p is 4.4 μm. Thus, results obtained using the lateral emission collection layout (see Figure 3.5a, marked as "Emission measurements") are in a good agreement with the theory which predicts that TIR occurs at the incident angle greater than 70.1°.

Figure 4.12a shows that the EW field reaches the surface when the STOF diameter is 82 μm and it increases as the diameter decreases to 55 μm. Because of the high porphyrin absorbance at the Soret band region, the EW is absorbed when it reaches the porphyrin layer, which leads to the decrease of the light intensity guided by the fiber. This results in two-fold lower fluorescence intensity at coned part with diameter of 35 μm, and no fluorescence between 25 and 15 μm waist since all excitation light is absorbed before the light reaches taper part with 25 μm diameter. Thus, according to the lateral emission measurements, the optimal diameter of tapered fiber is between 35 and 55 μm. This conclusion is also confirmed by the results shown in Figure 4.13 (obtained using the layout presented in Figure 3.5b). When the coned part with a diameter lower than 30 μm is immersed into toluene, there is almost no change in the porphyrin emission intensity. Thus, this tapered part of the fiber does not contribute to the fluorescence signal collected by the spectrometer. These measurements show that the optimal TOF diameter is close to 48 μm.

Summarizing the results of steady-state fluorescence studies discussed in this Section, the optimal diameter of the coned part of TOF has to be in the range between 35 μm (lateral measurements, Figure 4.12a) and 48 μm (toluene immersion measurements, Figure 4.13). Besides, as it is seen from Figure 4.12b, results obtained with the theoretical model which was used to calculate EW distribution along modified STOF, are in reasonable agreement with experimental data.

4.2.4 pH measurements

The main aim of the studies presented in [**III**] was to demonstrate the sensor application potentials of porphyrin functionalized STOFs. Porphyrins are known to undergo mono- and di-protonation in acidic media, which results in gradual change of both absorption and emission spectra [125]. To monitor emission spectrum change, the functionalized fiber was immersed into water solutions of hydrochloric acid, HCl, with pH from 0.05 to 4. In these experiments the scheme presented in Figure 3.5b was used. The STOF was successively immersed into media with different acidities for 20 s. During this period, the

(a) (b)

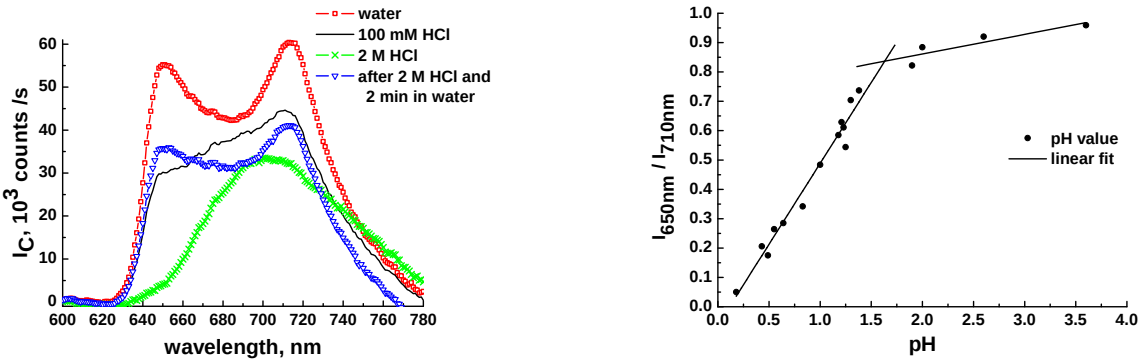

Figure 4.14: (a) The corrected emission spectra of the STOF with tip end diameter $d = 15$ μm. The fiber was successively immersed into water (squares), 100 mM HCl for one minute (smooth curve), 2 M HCl for one minute (crosses), and water for two minutes (triangles). (b) The dependence of the ratio of two emission maxima on the pH value for different concentrations of hydrochloric acid [**III**].

emission spectra were measured. After that, the tapered fiber was washed in water for 2 minutes and then the spectrum was recorded to verify the porphyrin layer recovery. Full recovery of the emission spectrum was observed down to pH values of 0.6. Two emission spectra of protonated porphyrin on STOF in 100 mM HCl (pH 1) and 2 M HCl (pH < 0.5) are shown in Figure 4.14a together with those corresponding to porphyrin SAM on STOF in pure water. These spectra reveal changes typical for the free-base porphyrin protonated forms. The initial fluorescence peaks at 648 and 718 nm were transformed into a peak at 710 nm for 100 mM HCl solution and then into a broad peak at 700 nm for 2 M HCl solution.

The obtained dependence of the ratio of emission intensities at 650 to 718 nm on pH of the solutions is shown in Figure 4.14b. It is worth mentioning that the protonation was reversible in hydrochloric acid down to pH value of 0.6, and only at the higher concentrations of the acid corresponding to pH < 0.6 the degradation of the optical sensor was observed. It is clearly seen from Figure 4.14b that the pH dependence is convincingly fitted with two linear approximations having a turning point at a pH value around 1.5. The linear fit from pH 3.8 to 1.6 can be ascribed to the mono-protonated state of the freebase porphyrin. The second linear approximation from pH 1.6 to 0.2 can be attributed to the di-protonated form of the free-base porphyrin. This phenomenon was previously shown by other researchers [105, 126]. The results clearly indicate that

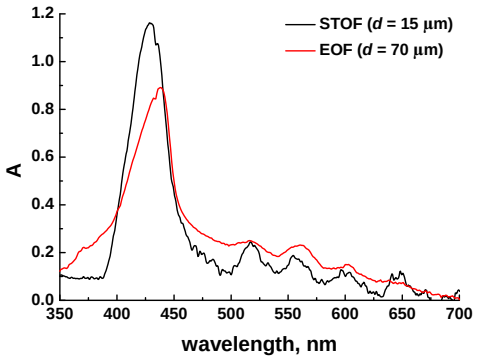

Figure 4.15: Typical absorption spectra of etched optical fiber (EOF) with $d = 70$ μm and STOF ($d = 15$ μm) modified with free-base porphyrin SAM.

modified STOF can be utilized as pH sensor in the range 0.6 – 3.8.

4.3 Etched optical fibers (EOFs)

Etched optical fibers (EOFs) were used for SAM deposition of free-base- and Zn-porphyrins, and modified yellow fluorescent protein (YFP).

4.3.1 Steady-state and time-resolved spectroscopy of porphyrin SAM films

In order to find out the optimum tip diameter of EOFs, optical fibers were etched down to various diameters: 35, 45, 55, and 70 μm. Then, EOFs were modified with free-base porphyrin using two steps scheme shown in Figure 3.2. Steady-state absorption spectra were recorded with the setup schematically shown in Figure 3.5a and marked as "Absorbance measurements". The studies revealed that EOFs with tip diameter 70 μm show quite reasonable absorbance at Soret and last two Q-bands when compared with STOFs (see Figure 4.15). In all further studies the 70 μm EOFs with transitional regions about 0.8 mm were used.

Emission spectrum studies were carried out with the setup shown in Figure 3.5b. In order to check the optimum tip length, EOF was immersed into toluene (since refractive index of toluene is higher than that of fiber core, there are significant light losses when EOF is immersed into toluene). The depth of immersion was controlled by micrometer screw with an accuracy of 0.5 mm. The results of these studies are presented in Figure 4.16b. As it is seen, there is a three-fold difference in spectrum intensities

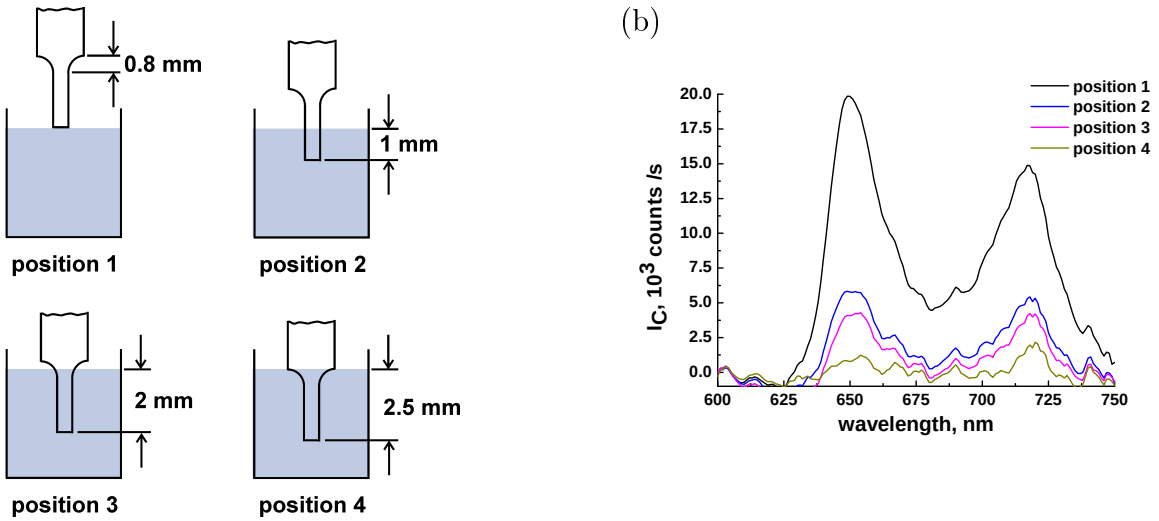

Figure 4.16: (a) Scheme showing positions of EOFs relative to air-toluene interface. (b) Emission spectra of modified EOF immersed into toluene down to various depths (see left-hand side Figure for details).

between EOF in air (Figure 4.16b, position 1) and immersed in toluene down to 1 mm (Figure 4.16b, position 2). Moreover, when EOF is immersed into toluene down to 2.5 mm, the fluorescence intensity of deposited porphyrins is vanishingly small (see Figure 4.16b, position 4). Therefore, the optimum parameters of modified EOFs for sensor applications are as follows: tip length 2.5 mm with corresponding tip diameter of 70 μm.

Time-resolved emission spectrum studies were carried out with the setup schematically presented in Figure 3.8c.The research showed that free-base porphyrin SAMs homogeneously cover surfaces of EOFs. The obtained fluorescence decay profiles were fitted with the three exponential model revealing the average weighted fluorescence lifetime to be 0.47 ± 0.001 ns.

In order to check the interaction of Zn ions with free-base porphyrin deposited on EOFs, the methanol solution of zinc acetate was prepared (MeOH : $Zn(O_2CCH_3)_2$ 40 mL : 400 mg). The emission spectra were recorded with the setup schematically shown in Figure 3.5b while EOF was immersed into the vial with solution in question. The obtained results revealed utterly small interaction of zinc with porphyrin monolayers (see Figure 4.17). One of the possible explanation for this phenomenon is that free-base porphyrin molecules form densely packed layers on surfaces of EOFs and hence, zinc ions have no access to porphyrin macrocycle for reaction to occur. The emission decrease in Figure 4.17 can be attributed to a photodegradation under laser irradiation.

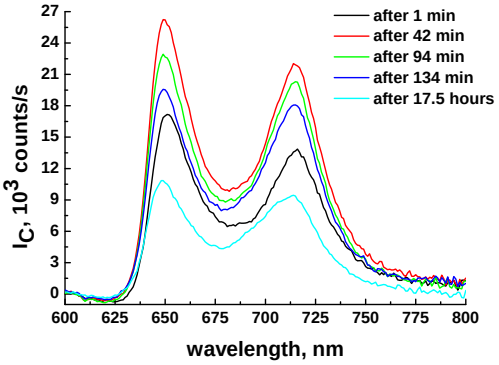

Figure 4.17: The emission spectra of modified EOFs when dipping into methanol solution of Zn acetate.

4.3.2 Diethylamine (DEA) steady-state and time-resolved measurements with Zn-porphyrin SAMs

(a) (b)

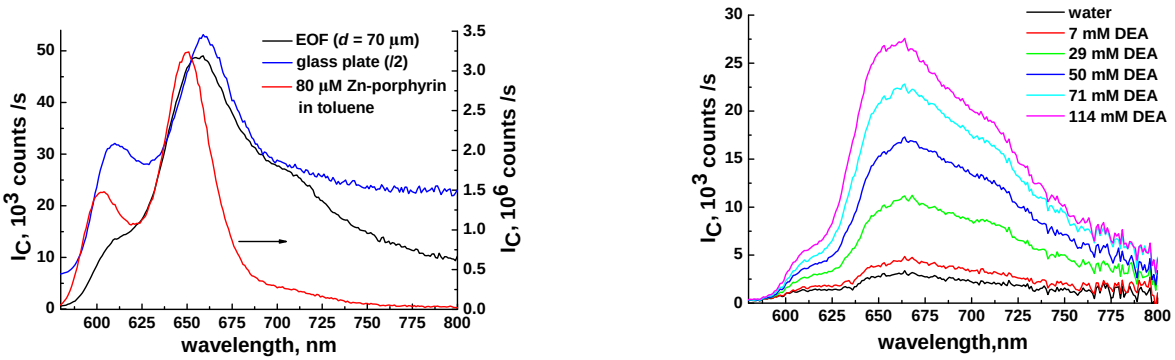

Figure 4.18: (a) Typical emission spectra of 80 μM solution of Zn-porphyrin in toluene (red curve, right Y-axis) and Zn-porphyrin SAMs on EOF (black curve, left Y-axis) and reference glass plate (blue curve, left Y-axis). (b) Emission spectra of EOF modified with Zn-porphyrin SAMs immersed into water solutions of diethylamine (DEA) at concentrations from 0 to 114 mM (indicated in the plot).

Zinc porphyrin SAMs were prepared using the same two steps procedure as that schematically shown in Figure 3.2 except for the Zn-porphyrin was used instead of free-base porphyrin. Typical corrected emission spectra of Zn-porphyrin SAMs on EOFs and glass plate, and its 80 μM solution in toluene are shown in Figure 4.18a. Emission spectrum of the glass plate was normalized to fit to the scale. It is worth mentioning that the spectra on EOFs and glass plate are in good agreement with that obtained

previously for Zn porphyrin on ITO surface, which had two emission peaks at 610 and 660 nm [79]. The first peak is not distinguishable for the EOF since a stronger emission from fiber itself was observed below 620 nm. The clear peak at around 720 nm for SAM on EOF (see Figure 4.18a, black curve) can be ascribed to the presence of small amount of free-base porphyrin in the stock solution of Zn-porphyrin. Indeed, very low peak at 720 nm can also be observed in the emission spectrum of the stock solution of Zn-porphyrin (Figure 4.18a, red curve). It should be also noted that the high level of emission intensity in the fluorescence spectrum of Zn-porphyrin SAM on glass plate (see Figure 4.18a, blue curve) for wavelengths higher than 700 nm, can be ascribed to background emission.

The FLM measurements of Zn-porphyrin films were not possible to carry out because of the low fluorescence lifetime of Zn-porphyrin in SAMs which is below the time resolution of used instrument (that is about 70 ps). Low fluorescence lifetime was previously reported for Zn-porphyrin SAMs in [79]. The quantum yield of fluorescence for Zn-porphyrin SAMs is at least one order of magnitude smaller than that for free-base porphyrin molecular layers. Because of this, it is possible to observe the emission peak at 720 nm from free-base porphyrin in the emission spectra of Zn-porphyrin SAMs (see Figure 4.18a), though the relative amount of free-base porphyrins in the layer can be rather low.

(a) (b)

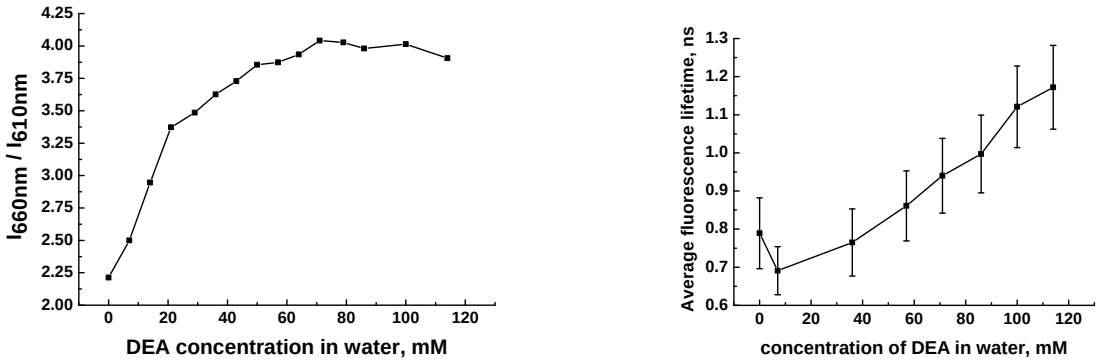

Figure 4.19: (a) The dependence of the ratio of emission intensities at 660 and 610 nm (for SAM of Zn-porphyrin on EOF) on different concentrations of DEA in water. (b) Dependence of measured average weighted fluorescence lifetime of Zn-porphyrin SAM on EOF, on various DEA concentrations. Inaccuracies of calculated values are shown with error bars.

Metalloporphyrins are known to change their absorption and emission spectra when

exposed to some volatile organic compounds such as diethylamine (DEA) [107]. Water solutions with different concentrations of DEA were studied with steady-state emission (Figure 3.5b) and time-resolved (Figure 3.6) spectroscopic techniques. The intensity of steady-state emission increases when DEA concentration raised from 7 to 114 mM (see Figure 4.18b). The dependence of the emission intensity ratio at 660 and 610 nm on the DEA concentration is demonstrated in Figure 4.19a. The ratio increases by 12 % when EOF is placed into 7 mM DEA solution and then further increases by 65 % when concentration is increased to 50 mM, but further concentration increase to 100 mM gives only 4 % rise in the ratio. This phenomenon can be explained by the saturation of the porphyrin SAM by DEA molecules, i.e. at DEA concentration of 50 mM almost all Zn-porphyrins in the layer form complexes with dissolved DEA and further growth of DEA concentration brings no change in complexation of DEA and Zn-porphyrin in SAMs.

The most probable reason for the increase of porphyrin fluorescence intensity in the presence of DEA molecules is coordination to central metal which reduces inter-porphyrin aggregation and thus, reduces self-quenching in molecular layer. In this case, the lifetime of the Zn-porphyrin excited state should also increase; this was confirmed by TCSPC studies (see Figure 4.19b). The average weighted fluorescence lifetimes were calculated with two exponential emission decay fits. When DEA concentration increases from 7 to 114 mM, the average fluorescence lifetime raises by 60 %. This change in DEA concentration corresponds to the emission ratio increase of roughly 65 % (see Figure 4.19a). It is also worth mentioning that the initial decrease of the average fluorescence lifetime for low concentration of DEA is within the inaccuracies (shown with error bars in Figure 4.19b) of obtained lifetime values.

4.3.3 Steady-state and time-resolved spectroscopy of YFP SAM films

To the best of our knowledge, so far there were no studies on EOFs functionalization with SAMs of fluorescent proteins. The modified YFP (or Citrine) SAMs were deposited following the procedure schematically presented in Figure 3.4 and described in Section 3.1.2. The steady-state absorption spectra were measured using the setup shown in Figure 3.5a, marked as “Absorbance measurements”. The studies revealed no detectable absorption on the glass samples, and relatively low absorbance at about 510 nm on the EOFs (Figure 4.20a). The wavelength of the absorption maximum, 514 nm, is consistent with that determined for Citrine in phosphate buffered saline (PBS) (see Figure 4.20a,

(a) (b)

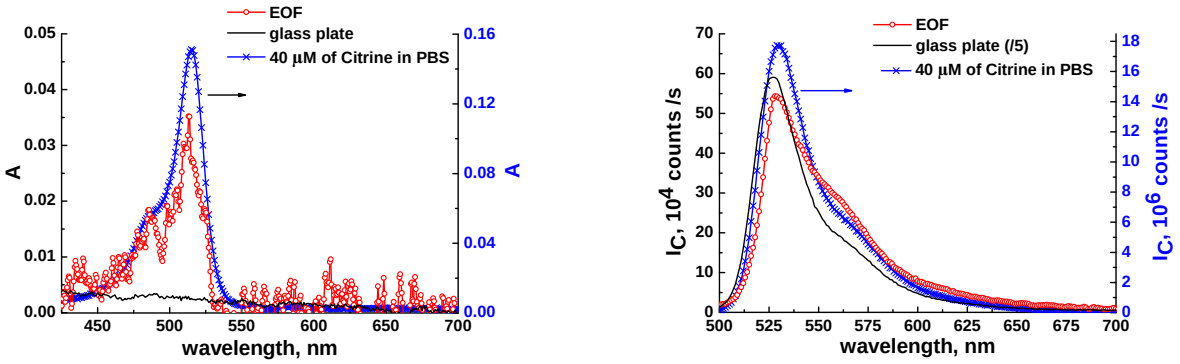

Figure 4.20: Absorption (a) and emission (b) spectra of EOF and reference glass plate modified with Citrine using SAM deposition technique. Spectra of the solution of 40 μM Citrine in phosphate buffered saline (PBS) with pH 7.4 are shown for comparison.

crosses).

The low absorbance of YFP on EOFs (when compared to that of free-base porphyrin SAMs on glass plates) is due to two reasons: i) the molar absorptivity, ϵ, of YFP (ε = 75000 $M^{-1}cm^{-1}$ [112]) is almost four times lower than that of free-base porphyrin (ε = 350000 $M^{-1}cm^{-1}$ [75]) and ii) mma of YFP SAM is higher than that of free-base porphyrin SAM which is 2.4 nm^2[75]. Indeed, absorbance for Citrine on glass plate at 515 nm is below noise signal, that is 0.0026 (see Figure 4.20a, black curve) and thus, taking into account $mma \geq (2 \cdot \varepsilon) / (N_A \cdot A)$, mma cannot be lower than 10 nm^2. This value is in reasonable agreement with the results obtained by Yang [127], and Ormö and co-authors [128] for GFP (in the buffer solution) for which diameter was estimated to be in the range 2.4 – 3 nm.

The steady-state emission measurements were carried out with the layout schematically shown in Figure 3.5b. The studies revealed a significant intensity of emission at 530 nm that is shown in Figure 4.20b. It can be ascribed to relatively high quantum yield of the fluorescence of studied YFPs (73 %) obtained previously in solution measurements [112]. A slight red shift for the emission peak on EOFs, as well as a higher value of emission intensity at 560 nm for the fiber, are due to the transmission properties of the dichroic mirror DM (see Figure 4.20b for details) rather then to actual difference in the emission spectra of the two SAMs.

The FLM measurements showed that proteins form morphologically homogeneous structures on EOFs and glass plates. Two typical FLM images are shown in Figure 4.21

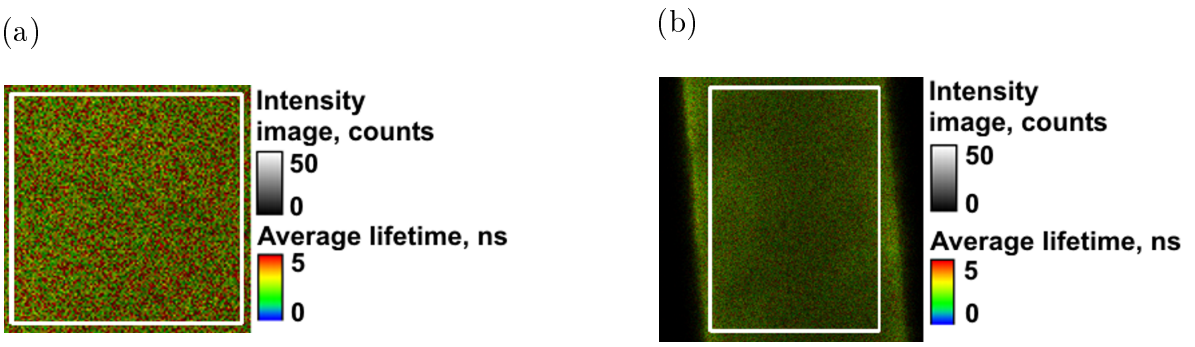

Figure 4.21: Typical FLM images revealing formation of YFP SAM layers on reference glass plate (a) and EOF (b). At each point of FLM image, brightness and colour denote intensity and average lifetime of molecular fluorescence, respectively. White rectangles show areas used to measure average weighted fluorescence lifetime [**V**].

and were obtained with the scheme presented in Figure 3.8c. Besides, the FLM measurements of non-modified YFP (which does not have Cys at the C-terminal) on glass plate revealed no fluorescence and therefore, it can be confirmed that the coupling occurred through the Cys residue. Hence, the coupling is site-specific and has covalent nature. The average weighted fluorescence lifetimes of YFP SAMs on the glass surface and EOF were calculated with bi-exponential fits of the emission decays. The average weighted fluorescence lifetimes of protein SAMs are 2.36 ± 0.20 and 2.40 ± 0.13 ns on the glass surfaces and EOFs, respectively. The two values are in a good agreement with each other. The main contributions to these values are from the short-lived components, which were 1.92 ns (69 %) for the EOF and 1.86 ns (68 %) for the glass sample. The longer-lived components were 3.44 and 3.41 ns and gave 31 % and 32 % contributions to the average weighted fluorescence lifetime values for EOF and glass plate, respectively. The obtained average weighted fluorescence lifetime values of YFPs deposited with SAM method on both surfaces are only 28 % shorter than that obtained previously for YFP in the buffer solution, 3.3 ns [112], indicating that dry conditions and protein aggregation have only minor effect on emission properties of YFP.

4.3.4 Effects of pH, Ca^{2+} ions, and proteases on YFP SAM films

Fluorescent proteins are known to be sensitive to pH of a medium as was demonstrated previously for GFP in pH range between 4 and 9 [110]. However, the effect of pH and other environmental factors on YFP SAMs deposited on EOFs have not been investigated yet. All steady-state emission spectra of modified EOFs in various environments were

studied with the setup shown in Figure 3.5b. Figure 4.22 presents the effect of pH on the fluorescence intensity of EOF at 530 nm. The fluorescence intensity decreases by 50 % at pH = 6 relative to its maximum at pH = 8.5. The fluorescent change is reversible in the pH range from 6.5 to 9 which is within the normal physiological range, but does not recover at all if the samples are immersed in solutions with pH below 4.

The observed degradation at low pH is similar to the previously reported studies on the pH stability of GFP in solutions [92, 129]. The reduction in the fluorescence intensity at the pH value below 5 can be attributed not only to the protonation of the chromophore, but also to conformational structural changes which occur close to the chromophore at low pH [92]. However, the ability to maintain the fluorescence in a reasonably broad range of pH enables pH sensor applications of the EOFs modified with SAMs of YFP.

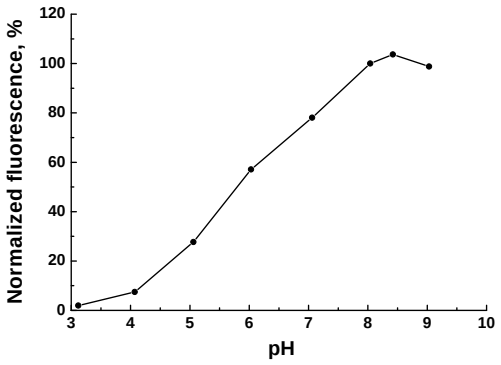

Figure 4.22: Dependence of the fluorescence intensity of EOF modified with YFP SAM on solution pH [**V**].

The fluorescent protein used in this Thesis had been previously used as genetically encoded Ca^{2+} indicator [110]. This promises another potential applications of EOFs modified with YFP SAMs as sensor of Ca^{2+} ions, which is one of the most important divalent cations present in the cell, as well as in many of the body fluids. As expected, the fluorescence intensity of EOF varied with different concentrations of calcium ions, as presented in Figure 4.23, showing the dependence of the emission intensity at 530 nm on Ca^{2+} concentrations. The presence of ions led to the increase of fluorescence intensity by roughly three folds until the concentration reached 15 mM, and it remained almost unchanged with further increase of the concentration of Ca^{2+} (see Figure 4.23 for more details). Importantly, the EOF modified with YFP SAMs can be used as calcium ion indicator even in μM ranges (Figure 4.23b).

The effects of various proteases on modified EOFs were studied using the setup schematically shown in Figure 3.5b. Stability of fluorescent proteins in the presence

(a) (b)

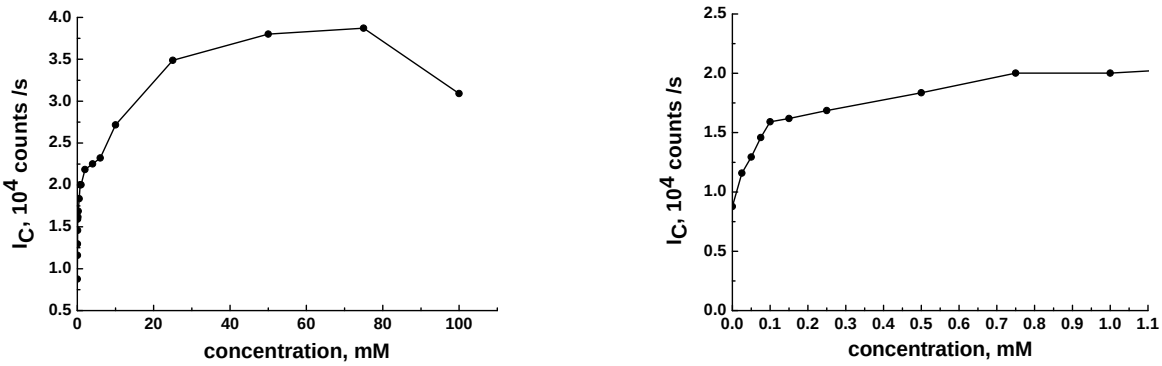

Figure 4.23: The effect of Ca^{2+} ions on emission intensity of EOF modified with YFP SAM film. The concentration ranges are (a) 0 – 100 mM and (b) 0 – 1.1 mM [**V**].

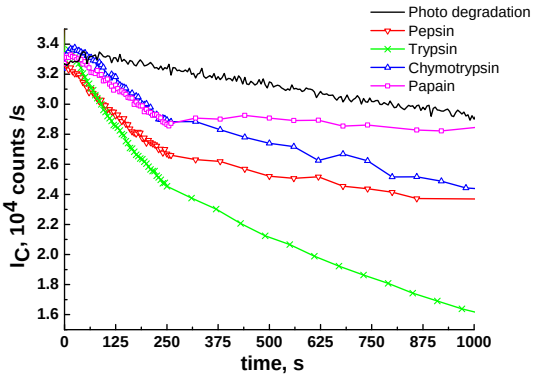

Figure 4.24: Effects of different proteases (concentrations 2 mg/mL) on the fluorescence of EOFs. Normalized corrected emission intensities are shown [**V**].

of various proteases was studied previously in solutions, and good resistivity of the protein to many proteases was reported [93, 127]. This was attributed to the fact that the chromophore is incorporated into protein body which has good resistivity to external agents [93]. Proteases such as pepsin, trypsin, chymotrypsin and papain at concentrations 2 mg/mL in PBS (pH 7.4) were used in this study. Upon the immersion in the corresponding solution (Figure 4.24), the initial decrease of fluorescence signal at 530 nm was observed for all the proteases. The fluorescence intensity stabilized, however, for all the solutions except for trypsin. The initial decrease in fluorescence intensity was about 13 % in 200 seconds. Some minor decrease in the fluorescence intensity at longer delays is mainly due to the photodegradation of YFP SAMs on EOFs (solid line in Figure 4.24). The variations in slopes for various curves are due to different fiber adjustments and

thus, different optical power densities at the EOF tips.

4.4 Hollow-core photonic bandgap fiber (HCPBGF). Steady-state and time-resolved fluorescence studies

Newly developed PCFs have an advantage of air-quartz interface in the area of wave propagation, at which a SAM can be deposited. This gives an opportunity to increase the efficiency of SAM–fiber guided light interaction. One part of this research work is reported in [**IV**] in which a hollow-core photonic bandgap fiber (HCPBGF) was used (Figure 3.1a). Free-base porphyrin was covalently attached to the surfaces of holes of HCPBGFs using two step self-assembling procedure schematically shown in Figure 3.2. The aims of the study were (i) to check the possibility to deposit porphyrin films inside the channels of PCFs using SAM technique, and (ii) to study the interaction of the electromagnetic field with the deposited molecules by monitoring emission spectra of the modified HCPBGFs. To the best of our knowledge, there were no experiments devoted to the porphyrin SAM covalent deposition inside HCPBGFs previously.

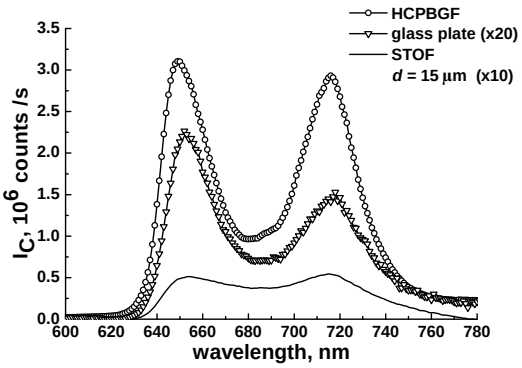

Figure 4.25: Corrected fluorescence spectra of free-base porphyrin SAMs covering the walls of the channels of HCPBGF (circles), STOF with $d = 15$ μm (smooth curve, multiplied by 10 to match the scale) and reference glass plate (triangles, multiplied by 20 to match the scale) [**IV**].

The emission spectrum studies of modified HCPBGFs were carried out with the setup schematically shown in Figure 3.5b. The corrected emission spectra of deposited porphyrins are shown in Figure 4.25. The spectrum measured for HCPBGF is virtually identical to that of porphyrin SAM on glass, and it is in good agreement with the spec-

tra obtained previously in [**III**] for STOFs. The emission spectrum of modified HCPBGF has much higher intensity than that of STOF. This difference can be explained by the following factors: (i) the optical losses are different for the two fibers (there are significant optical losses in the coned part of STOFs), ii) different amount of porphyrin fluorescence is reflected back into the cores of the two fibers, and (iii) the length from which emission can be collected is different for HCPBGF and STOF. The latter factor is due to various mechanisms of the excitation light interaction with deposited porphyrins. In HCPBGFs the excitation light is waveguided by the fiber, and it is directly absorbed by the photoactive molecules, whilst in STOFs the excitation of porphyrins is conducted via the interaction with EW field.

The porphyrin distribution inside HCPBGF channels was studied with FLM instrument. HCPBGF was cut into 15 mm long pieces to study each of them by FLM instrument. Each piece was scanned in 1 mm intervals. FLM images were obtained with the setups shown in Figure 3.8a and b. At each point on a FLM image, the brightness and the color denote the intensity and the average lifetime, respectively. The distributions of fluorescence intensity and lifetime revealed that (i) all the walls of HCPBGF channels were covered with porphyrin layers (Figure 4.26a, measured with the setup shown in Figure 3.8b), and (ii) porphyrins formed homogeneous SAMs inside HCPBGFs (Figure 4.26b, lower image, measured with the layout shown in Figure 3.8a).

In order to calculate the average weighted fluorescence lifetime, the measured emission decays were fitted using three exponential model. The average weighted fluorescence lifetime was found to be 1.82 ± 0.1 ns for the region indicated by the white rectangle in Figure 4.26b (lower image). The average lifetimes calculated for other regions of modified HCPBGF were essentially the same. This fluorescence lifetime is longer than that previously obtained for STOFs (0.36 ns) [**III**] for SAMs of exactly the same compound. It was also found out that the average emission lifetime depends on the pressure of nitrogen in PC, but without any strict correlation. A shorter fluorescence lifetime of porphyrin films is usually attributed to a higher degree of aggregation and thus, more efficient fluorescence self-quenching. Therefore, the difference in lifetimes can be interpreted as the lower density of porphyrins in the channels of HCPBGF as compared with that on STOF surfaces. Alternatively, the packing of porphyrins can be different when deposited from flowing solution (HCPBGF) and in steady conditions (STOF). At present we cannot conclude the exact reason for the longer lifetime, but from the practical point of view, the longer lifetime is beneficial for the ease of measurements and for fluorescence sensor applications.

(a)

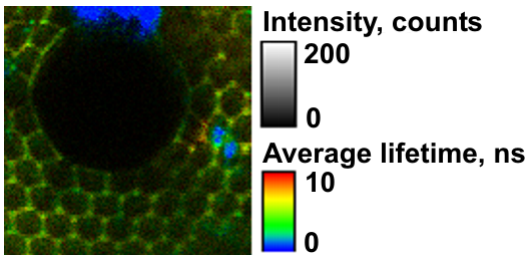

(b)

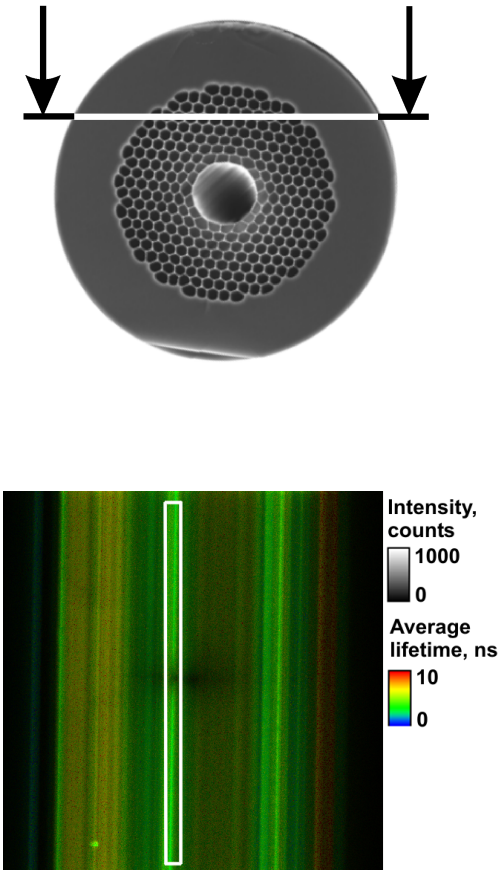

Figure 4.26: (a) A typical FLM image of HCPBGF cross-section with deposited free-base porphyrin SAMs. (b) The scheme showing the position of the cross-section scan (upper image) and a typical FLM image taken along HCPBGF with deposited free-base porphyrin SAMs (lower image). White rectangle shows the area used to obtain fluorescence lifetime decay curve [**IV**].

4.5 Solid-core photonic crystal fibers (SCPCFs)

4.5.1 Two-step free-base porphyrin SAMs

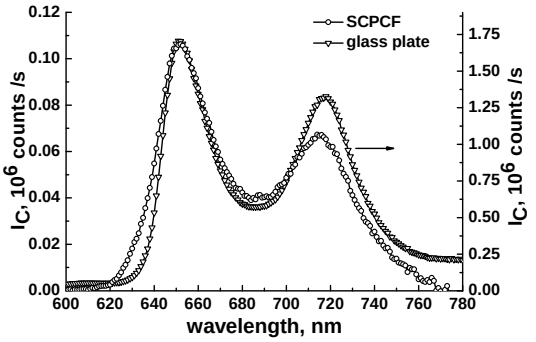

Figure 4.27: Typical emission spectra of SCPCF (circles, left Y-axis) and reference glass plate (triangles, right Y-axis) modified with free-base porphyrin by two-step SAM method.

SCPCFs were modified with free-base porphyrin SAMs using two-step procedure schematically shown in Figure 3.2. Emission spectra of SCPCF covered inside with porphyrin are presented in Figure 4.27. The emission spectra are in a good agreement with each other and similar to those obtained previously for SAMs on STOFs [**III**] revealing two maxima at 650 and 720 nm.

Measurements using FLM instrument revealed that all walls of the channels of modified SCPCF are covered with photoactive molecules (narrow green stripes in Figure 4.28a). The emission intensities in FLM cross-sectional image were too low to measure the fluorescence lifetime reliably, therefore longitudinal FLM images were recorded for the lifetime measurements. These studies were carried out with the setup shown schematically in Figure 3.8a, with 40× objective in place of 100× one. A representative longitudinal FLM image of modified SCPCF is shown in Figure 4.28b (lower image) together with the scheme showing the possible position of the cross-section scan (Figure 4.28b, upper image). The cross-section was selected in such way that three channels can be seen in the image (white rectangles show areas used to obtain fluorescence decay curves). In order to calculate the emission lifetime, the data were fitted using three exponential decay model. The measurements revealed that the lifetimes differ from channel to channel. The average fluorescence lifetime for central channel was found to be 0.72 ± 0.04 ns, while that for the left channel is 0.95 ± 0.05 ns and 0.82 ± 0.04 ns for the right channel. Therefore, the average over the three lifetimes is 0.83 ± 0.04 ns. This value is two

(a)

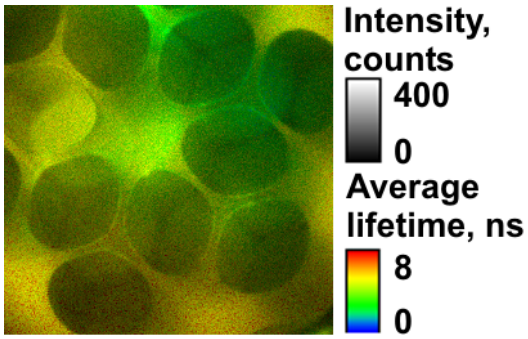

(b)

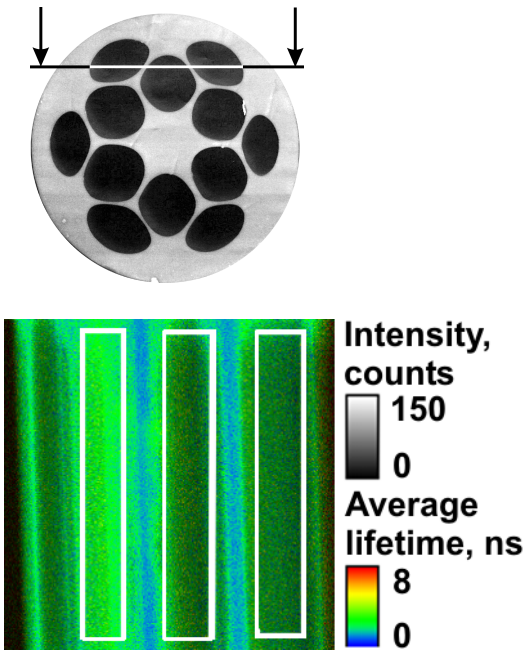

Figure 4.28: (a) A typical FLM image of SCPCF cross-section with deposited free-base porphyrin SAMs. (b) The scheme showing position of the longitudinal cross-section scan of SCPCF (upper image) and the corresponding FLM image (lower image). White rectangles show areas used to obtain fluorescence lifetime decay curves for different SCPCF channels.

times lower than that obtained for HCPBGFs and two times longer than that for STOF. This means that porphyrins are likely to be less aggregated than in the case of STOF samples, but more aggregated than in the channels of HCPBGFs. Most probably, the same nitrogen pressure in PC creates different flow rate of the reaction mixture through the channels for HCPBGF and SCPCF, and results in somewhat different density and aggregation degree of the porphyrins in the SAMs. It is also worth to mention that as in the case of modified HCPBGFs, the average weighted fluorescence lifetime depends on the pressure applied to PC during SAM deposition for the modified SCPCFs.

4.5.2 One-step free-base porphyrin SAMs. Metallation of the SAMs with Zinc

In order to simplify the SAM procedure, a series of compounds were synthesized in the Laboratory of Chemistry, Tampere University of Technology. These newly synthesized compounds, porphyrin and phthalocyanine derivatives, possess an anchor group which allows one-step covalent bonding to a quartz surface (see Figure 3.3) [118]. A porphyrin derivative from this series, mono(triethoxysilane) porphyrin (MTESP) was used to functionalize SCPCFs, the fibers which provide more flexibility for the light focusing when compared with HCPBGFs. For comparison, the same porphyrin was also deposited on a plane surface, quartz plate.

The typical emission spectra of SCPCF modified with MTESP (obtained with the setup schematically shown in Figure 3.5b) and MTESP on quartz plate are presented in Figure 4.29a. As it is seen, both spectra are in good agreement with each other, revealing two maxima at 650 and 715 nm.

Metallation of MTESP SAMs was studied in real-time by pumping Zn acetate (MeOH : $Zn(O_2CCH_3)_2$ 40 mL : 400 mg) through the channels of SCPCFs. During this procedure, the emission spectra were recorded every minute with the setup shown in Figure 3.5b. The obtained emission spectra are shown in Figure 4.29b. The results demonstrate that the reaction with Zn starts almost immediately after the liquid begins to flow through the fiber channels: the peak at 720 nm decreases, whilst a new band at 600 nm is formed (see Figure 4.29b, solid line). The similar result was obtained for quartz plates (the only difference is that plates were incubated for one hour in Zn acetate solution): there is no peak at 720 nm and a new band at 600 nm is formed (see Figure 4.29b, triangles). The maximum at 600 nm is typical for Zn-porphyrin SAMs, which was observed previously for EOFs (see Figure 4.18). It should be noted that the rise

(a) (b)

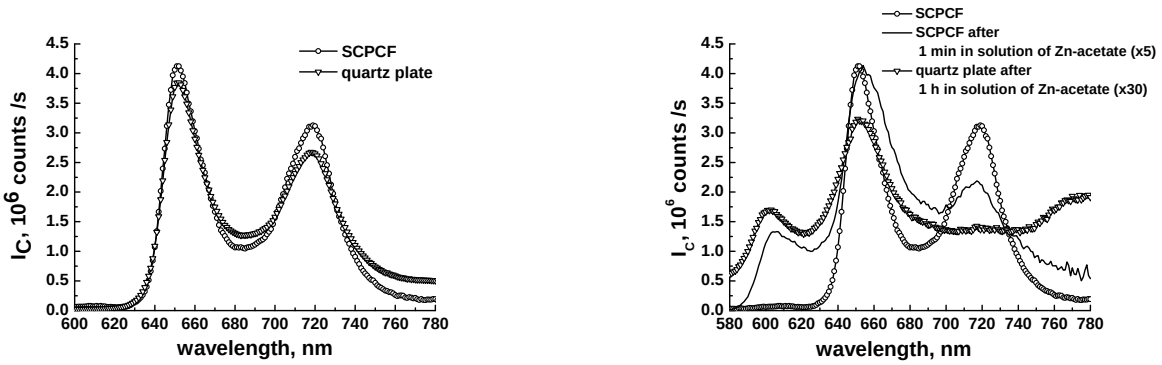

Figure 4.29: (a) Typical emission spectra of mono(triethoxysilane) porphyrin (MTESP) deposited with one-step SAM method inside the channels of SCPCF (circles) and on quartz plate (triangles). (b) Emission spectra of SCPCF modified with MTESP using one-step SAM method (circles), the same fiber after one minute in methanol solution of Zn acetate (solid line; multiplied by 5 to match the scale) and MTESP SAM on quartz plate after one hour in methanol solution of Zn acetate (triangles; multiplied by 30 to match the scale).

from 740 nm in the emission spectrum of SAM on quartz plate (Figure 4.29b, triangles) is a background emission, which was also visible for clean quartz plates. Monitoring of the 720 nm band disappearance can be used to study the reaction course. Surprisingly, although the initial metallation of SAM on SCPCF is fast, the band at 720 nm did not disappear completely even at very long reaction time (see Figure 4.29b, triangles). To understand this phenomenon the FLM measurements of modified fiber were carried out.

The cross-section FLM image revealed that photoactive molecules are deposited on the walls of all the channels of modified SCPCF (green stripes in Figure 4.30a), but the average lifetime differs from channel to channel. A representative longitudinal FLM image of modified SCPCF is shown in Figure 4.30b (lower image) together with the line marking the possible position of the scanned cross-section (Figure 4.30b, upper image). The cross-section was selected in such way that three channels can be seen in the image. The colors of the channels on FLM image are different and the corresponding average weighted fluorescence lifetimes are 0.87 ± 0.03 ns for the left channel, 0.46 ± 0.01 ns for the central channel, and 1.1 ± 0.04 ns for the right channel. The fluorescence lifetime of Zn-porphyrin SAM is shorter than that of free-base porphyrin SAM, and it can be concluded that the central channel is covered with the Zn-porphyrin SAM, while the two others are covered with the free-base porphyrin, MTESP. The most probable reason for

(a)

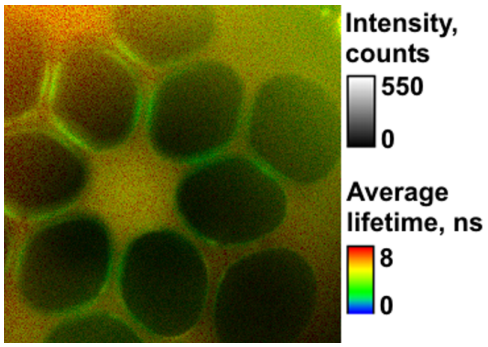

(b)

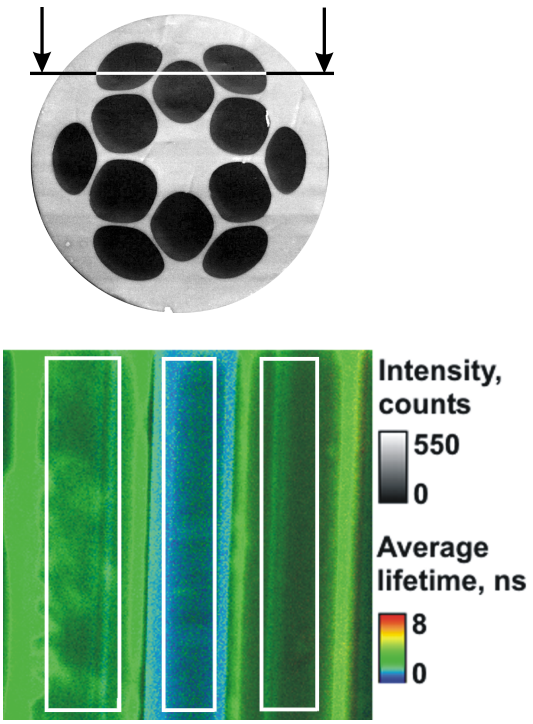

Figure 4.30: (a) Typical FLM image of SCPCF cross-section with metallated MTESP SAMs. (b) The scheme showing the position of the longitudinal cross-section scan (upper image) and the corresponding FLM image (lower image). One-step SAM deposition method was used. White rectangles show areas used to obtain fluorescence lifetime decay curves for different SCPCF channels.

this is that the left and right channels were blocked, for instance by dust particles, during the metallation of SAMs, as these channels are narrower and easier to block. The fact that not all the channels were available for Zn-metallation explains remaining emission band of free base porphyrin in the spectrum of modified SCPCF in Figure 4.29b.

4.6 Comparison of different fibers functionally enhanced by photoactive molecules

In this Thesis, the porphyrin SAMs were deposited on TOFs and EOFs, and inside the channels of various PCFs. This makes possible comparison of different fibers in order to establish relations between the fiber types and layer properties, and evaluate potentials of the fibers in sensor applications. The emission spectra of two-step free-base porphyrin SAMs measured from modified fibers are compared in Figure 4.31. The spectra are similar to each other and to those for reference glass plates (for comparison between STOF and glass plate see Figure 4.7b), but the intensities are rather different.

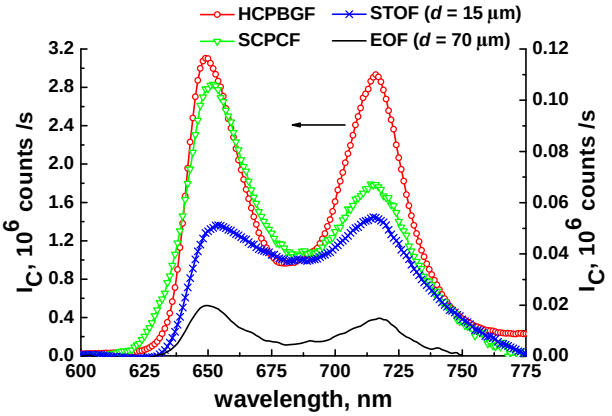

Figure 4.31: Typical emission spectra of STOF, EOF, and different PCFs modified with two-step SAMs of free-base porphyrin

The highest emission intensity was observed from HCPBGFs. It is reasonable result since the interaction with photoactive molecules occurs directly with the light propagating in the fiber channel and fluorescence is guided back directly by the hollow channel. Contrary to this, in STOFs, EOFs, and SCPCFs the interaction takes place by means of evanescent field which is much weaker than the light guided by the fiber core (see Figure 2.2). Besides, molecular fluorescence passes two (in case of STOFs and EOFs) or one (in case of SCPCFs) interface(s) between air and fiber materials in this kind of

Table 4.5: Comparison of average weighted fluorescence lifetimes, τ_{AV}, obtained for different types of fibers modified with two-step free-base porphyrin SAM method.

Sample	τ_{AV}, ns
Glass plate (reference to STOF)	0.30 ± 0.01
STOF ($d = 15$ μm)	0.36 ± 0.01
EOF ($d = 70$ μm)	0.47 ± 0.001
SCPCF	0.83 ± 0.04
HCPBGF	1.82 ± 0.1

fibers. Therefore, the measured fluorescence for SCPCFs is higher than that for STOFs and EOFs.

The length of tapered part of the fiber which has to be functionalized with photoactive molecular layer (in order to be used in sensor applications) was studied for STOFs and EOFs. The sufficient length is roughly 2 mm for EOF and at least 9 mm for STOF. This is resonable result since in case of EOF, the cladding is completely removed and photoactive molecules are deposited directly on the waveguiding core, whereas in the case of STOF the cladding is thinned (but still presents) thus reducing the efficiency of guided light interaction with the molecular layer. Unfortunately, similar measurements were not possible for PCFs. However, it can be expected that for HCPBGFs the sufficient functionalization length is even shorter than that for EOF, since the layer of photoactive molecules is in the waveguiding channel, and the diameter of the channel is smaller than that of EOF.

The average weighted fluorescence lifetimes obtained from time-resolved emission studies are summarized in Table 4.5. The lifetimes for STOFs and EOFs are in a good agreement with each other revealing only 30 % difference between these two fiber types. This is expected result since the experimental conditions in SAM process were similar. The fluorescence lifetime for HCPBGF is about 2.2 times higher than that obtained for SCPCF, and roughly 5 times higher than that for STOF. The proposed explanation for the differences in the fluorescence lifetimes is that porphyrins are more densely packed on STOFs than inside the two PCFs, and thus fluorescence self-quenching is more efficient in case of STOF and EOF. The longer lifetime means higher quantum yield of the porphyrin fluorescence, which is another important reason for observing high fluorescence intensity of HCPBGF as compared to other fibers.

Summarizing the obtained results of steady-state and time-resolved emission studies, highest fluorescence intensity and lifetime were observed for HCPBGFs. Therefore, this

kind of fibers would be of great interest in sensor applications. The EOFs sensors have an advantage of relatively simple fabrication procedure. Disadvantages of both SCPCF and HCPBGF are the need of pressure cell and poor control over pumping speed of reaction mixture during SAM process.

It is also interesting to compare EOFs modified with SAMs of free-base porphyrins and YFP SAMs. In spite of rather low molar absorptivity of YFP, the emission intensity of YFP SAMs is at least one order of magnitude higher than that of free-base porphyrin SAMs. It is mainly due to higher fluorescence quantum yield of modified YFP (73 % for Citrine in PBS solution [112]) compare to that of free-base porphyrin (11 % for 5,10,15,20-tetraphenylporphyrin in toluene [130]). Besides, the quenching due to aggregation is stronger for free-base porphyrin SAMs (0.5 ns relative to 10 ns for tetraphenylporphyrin in tetrahydrofuran [76]) as compared to that for YFP films (2.4 ns relative to 3.3 ns for YFP in PBS solution [112]). The comparison shows that emission quantum yield rather than layer absorption is important for obtaining high fluorescence intensity when measurements are carried out using scheme presented in Figure 3.5b, which is the scheme proposed for sensor applications. Though the length of SAM covering the fiber must be longer in the case of lower absorbing layer to consume the same amount of the excitation light. Summarizing the results of protein studies, EOFs with deposited layers of Citrine are promising choice for bio-sensor applications of modified optical fibers.

5 Concluding remarks

Based on the presented results the following conclusions have been made:

1. Different experimental setups were designed, assembled or adopted for the steady-state and time-resolved spectroscopy measurements of fibers functionally enhanced by the films of photoactive molecules. The role of modified optical fibers was twofold: i) delivery of the excitation light to the deposited layers of photoactive molecules, and ii) collection of the molecular fluorescence from these layers and its delivery to a measurement instrument.

2. The photoactive layers of porphyrins and yellow fluorescent proteins (YFPs) were deposited using Langmuir-Blodgett and self-assembled monolayer (SAM) methods. Experimental setups and tools for SAM deposition of the photoactive compounds on mechanically and chemically modified conventional optical fibers, and inside the channels of photonic crystal fibers (PCFs) were designed and constructed. This forms a platform for production and investigation of the functionalized optical fibers, studies of photoactive SAMs photophysical properties, and development of optical molecular sensors.

3. The optimum geometries of tapered (TOFs) and etched optical fibers (EOFs) for the efficient interaction of the evanescence field with the molecular layers deposited on their surfaces were determined by probing steady-state emission of the deposited molecular layers along the fibers under study. Summarizing the obtained results, the optimum tip diameter of a TOF is $35-48$ μm for fibers with 105 μm core and 125 μm cladding diameters. For chemically EOFs a sufficient etching length was found to be 2.5 mm with corresponding tip diameter of 70 μm.

4. The deposition time of two-step SAM procedure of free-base porphyrin attachment to glass surfaces was studied and optimized. The developed experimental optical setup and reaction cell made it possible to carry out real-time measurements of porphyrin attachment during SAM process and to determine that the free-base

porphyrin SAM formation is completed within one hour. This experimental setup can be used for the time optimization of the SAM process independent of the type of photoactive molecules in question.

5. Four different types of optical fibers were studied and optimized for their possible molecular sensor applications. The most promising results were obtained for PCFs, which delivered the highest fluorescence intensity of the SAM probe to the detection system. Besides, this kind of optical fibers have highest measured emission lifetime making them the best choice (among other studied modified optical fibers) in sensor applications. The main disadvantages of PCFs are the need of pressure cell and poor control over pumping speed of reaction mixture during SAM process. Chemically etched fibers are relatively easy to manufacture and the SAM deposition reproducibility is among the best for studied fiber samples. The fluorescence intensity collected from these fibers is reasonably high, which makes them good candidates for simple sensor applications. TOFs can also be used in similar applications, but the length of TOF coned part on which photoactive molecules are to be deposited, is much longer than that for EOF. This makes TOFs more fragile and difficult to use.

6. The optical fiber sensor applications were demonstrated using a few types of porphyrin and Citrine (modification of YFP) SAMs as analyte probes. The most successful results were obtained for pH measurements (with free-base porphyrin and Citrine probes), detection of calcium ions (Citrine probe), and monitoring of diethylamine (Zn-porphyrin probe). Based on the developed platform other photoactive SAM probes can be studied to find their applications in the field of optical fiber sensors.

Bibliography

[1] H. Imahori, T. Umeyama, and S. Ito. Large /*pi*-aromatic molecules as potential sensitizers for highly efficient dye-sensitized solar cells. *Acc. Chem. Res.*, 42 (11): 1809–1818, 2009.

[2] G. Bottari, G. Torre, D. M. Guldi, and T. Torres. Covalent and noncovalent phthalocyanine–carbon nanostructure systems: synthesis, photoinduced electron transfer, and application to molecular photovoltaics. *Chem. Rev.*, 11:6768–6816, 2010.

[3] J. E. Debs, H. Ebendorff-Heidepriem, J. S. Quinton, and T. M. Monro. A fundamental study into the surface functionalization of soft glass microstructured optical fibers via silane coupling agents. *J. Lightwave Technol.*, 27:576–582, 2009.

[4] F. Benabid, F. Couny, J. C. Knight, T. A. Birks, and P. St. J. Russell. Compact, stable and efficient all–fibre gas cells using hollow–core photonic crystal fibres. *Nature*, 434:488–491, 2005.

[5] J. S. Y. Chen, T. G. Euser, N. J. Farrer, P. J. Sadler, M. Scharrer, and P. St. J. Russell. Photochemistry in photonic crystal fiber nanoreactors. *Chem. Eur. J.*, 16:5607–5612, 2010.

[6] T. Hasan, Z. Sun, F. Wang, F. Bonaccorso, P. H. Tan, A. G. Rozhin, and A. C. Ferrari. Nanotube–polymer composites for ultrafast photonics. *Adv. Mater.*, 21: 3874–3899, 2009.

[7] F. Benabid, J. C. Knight, and P. St. J. Russell. Particle levitation and guidance in hollow–core photonic crystal fiber. *Opt. Exp.*, 10:1195–1203, 2002.

[8] A.W. Snyder and J.D. Love. *Optical Waveguide Theory*. Kluwer Academic Publishers, Norwell, Massachusstes, 2000.

[9] D. Marcuse. Loss analysis of single–mode fiber splices. *Bell Syst. Tech. J.*, 56: 703–718, 1977.

[10] N. Nath and S. Anand. Evanescent wave fiber optic fluorosensor: effect of tapering configuration on the signal acquisition. *Opt. Eng.*, 37(1):220–228, 1998.

[11] G. S. Vasylevska, S. M. Borisov, C. Krause, and O. S. Wolfbeis. Indicator–loaded permeation–selective microbeads for use in fiber optic simultaneous sensing of pH and dissolved oxygen. *Chem. Mater.*, 18:4609–4616, 2006.

[12] E. J. Park, K. R. Reid, W. Tang, R. T. Kennedy, and R. Kopelman. Ratiometric fiber optic sensors for the detection of inter– and intra–cellular dissolved oxygen. *J. Mater. Chem.*, 15:2913–2919, 2005.

[13] M. Ahmad, K.-P. Chang, T. A. King, and L. L. Hench. A compact fibre–based fluorescence sensor. *Sens. Act. A*, 119:84–89, 2005.

[14] J. Moreno, F. J. Arregui, and I. R. Matias. Fiber optic ammonia sensing employing novel thermoplastic polyurethane membranes. *Sens. Act. B*, 105:419–424, 2005.

[15] S. Korposh, S. Kodaira, S. W. Lee, W. J. Batty, S. W. James, and R. P. Tatam. Fabrication of sensitive fibre–optic gas sensors based on nano–assembled thin films. In *IEEE SENSORS 2008 Conference, Lecce, Italy*, 26-29 October, 2008.

[16] S. Khalil, L. Bansal, and M. El-Sherif. Intrinsic fiber optic chemical sensor for the detection of dimethyl methylphosphonate. *Opt. Eng.*, 43 (11):2683–2688, 2004.

[17] P. V. Preejith, C. S. Lim, and T. F. Chia. Serum protein measurement using a tapered fluorescent fibre–optic evanescent wave–based biosensor. *Meas. Sci. Technol.*, 17:3255–3260, 2006.

[18] J. M. Corres, I. R. Matias, J. Bravo, and F. J. Arregui. Tapered optical fiber biosensor for the detection of anti–gliadin antibodies. *Sens. Act. B*, 135:166–171, 2008.

[19] H.S. Haddock, P.M. Shankar, and R. Mutharasan. Evanescent sensing of biomolecules and cells. *Sens. Act. B*, 88:67–74, 2003.

[20] M. Rusu, S. Kivisto, C. B. E. Gawith, and O. G. Okhotnikov. Red–Green–Blue (rgb) light generator using tapered fiber pumped with a frequency–doubled Yb–fiber laser. *Opt Expr*, 13(21):8547–8554, 2005.

[21] R. Gumenyuk, C. Thur, S. Kivisto, and O. G. Okhotnikov. Tapered fiber bragg gratings for dispersion compensation in mode–locked Yb–doped fiber laser. *IEEE J. Quantum Elect.*, 46:769–773, 2010.

[22] S. Pilevar, C. C. Davis, and F. Portugal. Tapered optical fiber sensor using near–infrared fluorophores to assay hybridization. *Anal. Chem.*, 70:2031–2037, 1998.

[23] T. E. Dimmick, G. Kakarantzas, T. A. Birks, and P. St. J. Russell. Carbon dioxide laser fabrication of fused–fiber couplers and tapers. *Applied Optics*, 38 (33):6845–6848, 1999.

[24] C. D. Hussey and J. D. Minelly. Optical fibre polishing with a motor–driven polishing wheel. *Electr. Lett.*, 24(13):805–807, 1988.

[25] A. Gaston, F. Perez, and J. Sevilla. Optical fiber relative–humidity sensor with polyvinyl alcohol film. *Appl. Optics*, 43 (21):4127, 2004.

[26] M. Lomer, J. Arrue, C. Jauregui, P. Aiestaran, J. Zubia, and J. M. Lopez-Higuera. Lateral polishing of bends in plastic optical fibres applied to a multipoint liquid–level measurement sensor. *Sens. Act. A*, 137:68–73, 2007.

[27] Y. Zaatar, D. Zaouk, J. Bechara, A. Khoury, C. Llinaress, and J. P. Charles. Fabrication and characterization of an evanescent wave fiber optic sensor for air pollution control. *Mater. Sci. Eng. B*, 74:296–298, 2000.

[28] H. S. Haddock, P. M. Shankar, and R. Mutharasan. Fabrication of biconical tapered optical fibers using hydrofluoric acid. *Mater. Sci. Eng. B*, 97:87–93, 2003.

[29] P. Hoffmann, B. Dutoit, and R. P. Salathe. Comparison of mechanically drawn and protection layer chemically etched optical fiber tips. *Ultramicroscopy*, 61:165–170, 1995.

[30] P. St. J. Russell. Photonic crystal fibers. *Science*, 299(5605):358–362, 2003.

[31] D. J. Brink and M. E. Lee. Confined blue iridescence by a diffracting microstructure: an optical investigation of the Cynandra opis butterfly. *Appl. Opt.*, 38(25): 5282–5289, 1999.

[32] M. G. Istvan, G. I. Márk, Z. Vértesy, K. Kertész, K. Ratter, Z. Bálint, and L. P. Biró. Ordered and disordered biological and biomimetic photonic nanoarchitectures. In *Fourth International Conference on Optical, Optoelectronic and Photonic*

Materials and Applications (ICOOPMA 2010), Budapest, Hungary, 15-20 August, 2010.

[33] P. St. J. Russell. Photonic–crystal fibers. *J. Lightwave Technol.*, 24(12):4729–4749, 2006.

[34] J. D. Joannopoulus, S. G. Johnson, J. N. Winn, and R. D. Meade. *Photonic crystals. Molding the flow of light.* Princeton University Press, Princeton, 2nd edition edition, 2008. URL `http://ab-initio.mit.edu/book/photonic-crystals-book.pdf`.

[35] S. Jr. Arismar Cerqueira. Recent progress and novel applications of photonic crystal fibers. *Rep. Prog. Phys.*, 73:024401–024422, 2010.

[36] V. V. Ravi Kanth Kumar, A. K. George, W. H. Reeves, J. C. Knight, P. St. J. Russell, F. G. Omenetto, and A. J. Taylor. Extruded soft glass photonic crystal fiber for ultrabroad supercontinuum generation. *Opt. Expr.*, 10(25):1520–1525, 2002.

[37] V. V. Ravi Kanth Kumar, A. K. George, J. C. Knight, and P. St. J. Russell. Tellurite photonic crystal fiber. *Opt. Expr.*, 11(20):2641–2645, 2003.

[38] Z. G. Lian, Q. Q. Li, D. Furniss, T. M. Benson, and A. B. Seddon. Solid microstructured chalcogenide glass optical fibers for the near– and mid–infrared spectral regions. *IEEE Photonic. Tech. L.*, 21(24):1804–1806, 2009.

[39] M. C. J. Large, S. Ponrathnam, A. Argyros, I. Bassett, N. S. Punjari, F. Cox, G. W. Barton, and M. A. van Eijkelenborg. Microstructured polymer optical fibres: new opportunities and challenges. *Mol. Cryst. Liq. Cryst.*, 446:219–231, 2006.

[40] R. T. Bise and D. J. Trevor. Sol–gel derived microstructured fiber: fabrication and characterization. In *Optical Fiber Communication Conference, Anaheim, USA. 6-11 March 2005*, volume 3, page OWL6, 2005.

[41] J.C. Knight, J. Broeng, T.A. Birks, and P.St.J. Russell. Photonic band gap guidance in optical fibers. *Science*, 282(5393):1476–1478, 1998.

[42] J. C. Knight, T. A. Birks, P. St. J. Russell, and D. M. Atkin. All–silica single–mode optical fiber with photonic crystal cladding. *Opt. Lett.*, 21(19):1547–1549, 1996.

[43] P. J. Roberts, F. Couny, H. Sabert, B. J. Mangan, D. P. Williams, L. Farr, M. W. Mason, and A. Tomlinson. Ultimate low loss of hollow–core photonic crystal fibres. *Opt. Expr.*, 13:236–244, 2005.

[44] G. Decher and J. D. Hong. Buildup of ultrathin multilayer films by a self-assembly process, (1) consecutive adsorption of anionic and cationic bipolar amphiphiles on charged surfaces. *Makromol. Chem., Macromol. Symp.*, 46:321–327, 1991.

[45] P. T. Hammond. Recent explorations in electrostatic multilayer thin film assembly. *Curr. Opin. Colloid In.*, 4:430–442, 2000.

[46] G. L. Gaines. *Insoluble monolayers at liquid–gas interfaces.* Interscience, New York, 1966.

[47] R. H. Tredgold. The physics of Langmuir–Blodgett films. *Rep. Prog. Phys.*, 50: 1609–1656, 1987.

[48] A. Ulman. *An introduction to ultrathin organic films: from Langmuir–Blodgett to self–assembly.* Academic Press, Boston, 1991.

[49] D. K. Schwartz. Mechanisms and kinetics of self-assembled monolayer formation. *Ann. Rev. Phys. Chem.*, 52(1):107–137, 2001.

[50] P. K. Iler. Multilayers of colloidal particles. *J. Colloid Sci.*, 21:569–594, 1966.

[51] C. W. Tse, K. Y. K. Man, K. W. Cheng, C. S. K. Mak, W. K. Chan, C. T. Yip, Z. T. Liu, and A. B. Djurisic. Layer–by–Layer deposition of Rhenium–containing hyperbranched polymers and fabrication of photovoltaic cells. *Chem. Eur. J.*, 13(1):328–335, 2007.

[52] X. Qu and T. Komatsu. Molecular capture in protein nanotubes. *ACS Nano*, 4(1): 563–573, 2010.

[53] Y. Egawa, R. Hayashida, and J. Anazai. Multilayered assemblies composed of brilliant yellow and poly(allylamine) for an optical pH sensor. *Anal. Sci.*, 22: 1117–1119, 2006.

[54] A. A. Mamedov, A. Belov, M. Giersig, N. N. Mamedova, and N. A. Kotov. Nanorainbows: graded semiconductor films from quantum dots. *J. Am. Chem. Soc.*, 123:7738–7739, 2001.

[55] A. Ulman. Formation and structure of self–assembled monolayers. *Chem. Rev.*, 96:1533–1554, 1996.

[56] L. S. Wong, F. Khan, and J. Micklefield. Selective covalent protein immobilization: strategies and applications. *Chem. Rev.*, 109:4025–4053, 2009.

[57] A. Badia, S. Singh, L. Demers, L. Cuccia, G. R. Brown, and R. B. Lennox. Self–assembled monolayers on gold nanoparticles. *Chem. Eur. J.*, 2(3):359–363, 1996.

[58] G. E. Poirier and E. D. Pylant. The self–assembly mechanism of alkanethiols on Au(111). *Science*, 272(5265):1145–1148, 1996.

[59] H. Ogawa, T. Chihara, and K. Taya. Selective monomethyl esterification of dicarboxylic acids by use of monocarboxylate chemisorption on alumina. *J. Am. Chem. Soc.*, 107(5):1365–1369, 1985.

[60] M. G. Samant, C. A. Brown, and J. G. Gordon. An epitaxial organic film. the self-assembled monolayer of docosanoic acid on silver(111). *Langmuir*, 9:1082–1085, 1993.

[61] I. M. Tidswell, B. M. Ocko, P. S. Pershan, S. R. Wasserman, G. M. Whitesides, and G. D. Axe. X–ray specular reflection studies of silicon coated by organic monolayers (alkylsiloxanes). *Phys. Rev. B*, 41(2):1111–1128, 1990.

[62] N. S. Enikolopyan. *Porphiriny. Struktura, svojstva, sintez (in Russian).* Nauka, Moscow, 1985.

[63] S. J. A. Gisbergen van, A. Rosa, G. Ricciardi, and E. J. Baerends. Time–dependent density functional calculations on the electronic absorption spectrum of free base porphin. *J. Chem. Phys.*, 111(6):2499–2506, 1999.

[64] E. D. Sternberg, D. Dolphin, and C. Bruckner. Porphyrin-based photosensitizers for use in photodynamic therapy. *Tetrahedron*, 54:4151–4202, 1998.

[65] M. Biesaga, K. Pyrzynska, and M. Trojanowicz. Porphyrins in analytical chemistry. A review. *Talanta*, 51:209–224, 2000.

[66] M. R. Wasielewski. Photoinduced electron transfer in supramolecular systems for artificial photosynthesis. *Chem. Rev.*, 92:435–461, 1992.

[67] H. Imahori. Giant multiporphyrin arrays as artificial light–harvesting antennas. *J. Phys. Chem. B*, 108:6130–6143, 2004.

[68] A. D'Amico, C. D. Natale, R. Paolesse, A. Macagnano, and A. Mantini. Metalloporphyrins as basic material for volatile sensitive sensors. *Sens. Act. B*, 65: 209–215, 2000.

[69] N. A. Rakow and K. S. Suslick. A colorimetric sensor array for odour visualization. *Nature*, 406:710–713, 2000.

[70] L. Baldini, A. J. Wilson, J. Hong, and A. D. Hamilton. Pattern–based detection of different proteins using an array of fluorescent protein surface receptors. *J. Am. Chem. Soc.*, 126:5656–5657, 2004.

[71] C.D. Natale, R. Paolesse, and A. D'Amico. Metalloporphyrins based artificial olfactory receptors. *Sens. Act. B*, 121(1):238–246, 2007.

[72] D. W. J. McCallien, P. L. Burn, and H. L. Anderson. Chelation of diamine ligands to zinc porphyrin monolayers amide–linked to glass. *J. Chem. Soc., Perkin Trans.*, 1:2581–2586, 1997.

[73] A. Gulino, P. Mineo, E. Scamporrino, D. Vitalini, and I. Fragal. Spectroscopic and microscopic characterization and behavior of an optical pH meter based on a functional hybrid monolayer molecular system: porphyrin molecules covalently assembled on a molecularly engineered silica surface. *Chem. Mat.*, 18(9):2404–2410, 2006.

[74] T. Hasobe, H. Imahori, K. Ohkubo, H. Yamada, T. Sato, Y. Nishimura, I. Yamazaki, and S. Fukuzumi. Structure and photoelectrochemical properties of ITO electrodes modified with self–assembled monolayers of meso, meso-linked porphyrin oligomers. *JPP*, 7(5):296–312, 2003.

[75] V. Chukharev, T. Vuorinen, A. Efimov, N. V. Tkachenko, M. Kimura, S. Fukuzumi, H. Imahori, and H. Lemmetyinen. Photoinduced electron transfer in self–assembled monolayers of porphyrin-fullerene dyads on ITO. *Langmuir*, 21:6385–6391, 2005.

[76] H. Imahori, K. Hosomizu, Y. Mori, T. Sato, T. K. Ahn, S. K. Kim, D. Kim, Y. Nishimura, I. Yamazaki, H. Ishii, H. Hotta, and Y. Matano. Substituent effects

of porphyrin monolayers on the structure and photoelectrochemical properties of self–assembled monolayers of porphyrin on ITO electrode. *J. Phys. Chem. B*, 108: 5018–5025, 2004.

[77] H. Yamada, H. Imahori, Y. Nishimura, I. Yamazaki, T. K. Ahn, S. K. Kim, D. Kim, and S. Fukuzumi. Photovoltaic properties of self–assembled monolayers of porphyrins and porphyrin–fullerene dyads on ITO and gold surfaces. *J. Am. Chem. Soc.*, 125:9129–9139, 2003.

[78] H. Yamada, H. Imahori, Y. Nishimura, I. Yamazaki, and S. Fukuzumi. Remarkable enhancement of photocurrent generation by ITO electrodes modified with a self–assembled monolayer of porphyrin. *Chem. Commun.*, pages 1921–1922, 2000.

[79] M. Isosomppi, N. V. Tkachenko, A. Efimov, K. Kaunisto, K. Hosomizu, H. Imahori, and H. Lemmetyinen. Photoinduced electron transfer in multilayer self–assembled structures of porphyrins and porphyrin–fullerene dyads on ITO. *J. Mater. Chem.*, 15:4546–4554, 2005.

[80] H. Imahori, H. Norieda, Y. Nishimura, I. Yamazaki, K. Higuchi, N. Kato, T. Motohiro, H. Yamada, K. Tamaki, M. Arimura, and Y. Sakata. Chain length effect on the structure and photoelectrochemical properties of self–assembled monolayers of porphyrins on gold electrodes. *J. Phys. Chem. B*, 104:1253–1260, 2000.

[81] A. V. Efimov, M. Anikin, N. V. Tkachenko, A. F. Mironov, and H. Lemmetyinen. Irregular behavior of 5,10,15,20-tetrakis(pentafluorophenyl)porphyrin in Langmuir–Blodgett films. *Chem. Phys. Lett.*, 289:572–578, 1998.

[82] D. G. Zhu, D. F. Cui, M. C. Petty, and M. Harris. Gas sensing using Langmuir–Blodgett films of a Ruthenium porphyrin. *Sens. Act. B*, 12:111–114, 1993.

[83] S. K. Lee and I. Okura. Photostable optical oxygen sensing material: platinumtetrakis(pentafluorophenyl)porphyrin immobilized in polystyrene. *Anal. Comm.*, 34: 185–188, 1997.

[84] R. Y. Tsien. The Green Fluorescent Protein. *Annu. Rev. Biochem.*, 67:509–544, 1998.

[85] N.C. Shaner, P.A. Steinbach, and R.Y. Tsien. A guide to choosing fluorescent proteins. *Nature Methods*, 2:905–909, 2005.

[86] A. Miyawaki, J. Llopis, R. Heim, J. M. McCaffery, J. A. Adams, M. Ikurak, and R. Y. Tsien. Fluorescent indicators for Ca^{2+} based on Green Fluorescent Proteins and Calmodulin. *Nature*, 388:882–887, 1997.

[87] M. Losche. Protein monolayers at interfaces. *Curr. Opin. Solid St. M.*, 2:546–556, 1997.

[88] R.K. Smith, P.A. Lewis, and P.S. Weiss. Patterning self-assembled monolayers. *Prog. Surf. Sci.*, 75:1–68, 2004.

[89] A. Bernard, J. P. Renault, B. Michel, H. R. Bosshard, and E. Delamarche. Microcontact printing of proteins. *Adv. Mater.*, 12(14):1067–1070, 2000.

[90] C. Nicolini. Protein–monolayer engineering: principles and application to biocatalysis. *Trends Biotechnol.*, 15(10):395–401, 1997.

[91] H. B. Lu, J. Homola, C. T. Campbell, G. G. Nenninger, S. S. Yee, and B. D. Ratner. Protein contact printing for a surface plasmon resonance biosensor with on–chip referencing. *Sens. Act. B*, 74:91–99, 2001.

[92] T. N. Campbell and F. Y. M. Choy. The effect of pH on green fluorescent protein: a brief review. *Mol. Biol. Today*, 2:1–4, 2001.

[93] C. Chiang, D. T. Okou, T. B. Griffin, C. R. Verret, and M. N. V. Williams. Green Fluorescent Protein rendered susceptible to proteolysis: positions for protease–sensitive insertions. *Arch. Biochem. Biophys.*, 394(2):229–235, 2001.

[94] C. McDonagh, C. S. Burke, and B. D. MacCraith. Optical chemical sensors. *Chem. Rev.*, 108:400–422, 2008.

[95] S. M. Borisov and O. S. Wolfbeis. Optical biosensors. *Chem. Rev.*, 108:423–461, 2008.

[96] R. J. Myers. One–hundred years of pH. *J. Chem. Educ.*, 87(1):30–32, 2010.

[97] J. Goicoechea, C. R. Zamarreno, I. R. Matias, and F. J. Arregui. Optical fiber pH sensors based on layer–by–layer electrostatic self–assembled Neutral Red. *Sens. Act. B*, 132:305–311, 2008.

[98] W. Tan, Z. Y. Shi, and R. Kopelman. Development of submicron chemical fiber optic sensors. *Anal. Chem.*, 64:2985–2990, 1992.

[99] T. Vo-Dinh. Nanosensing at the single cell level. *Spectrochim. Acta Part B*, 63: 95–103, 2008.

[100] M. M. Martin and L. Lindqvist. The pH dependence of fluorescein fluorescence. *J. Lumin.*, 10(6):381–390, 1975.

[101] J. E. Whitaker, R. P. Haugland, and F. G. Prendergast. Spectral and photophysical studies of benzo[c]xanthene dyes: Dual emission pH sensors. *Anal. Biochem.*, 194(2):330–344, 1991.

[102] A. S. Vasylevska, A. A. Karasyov, S. M. Borisov, and C. Krause. Novel coumarin–based fluorescent pH indicators, probes and membranes covering a broad pH range. *Anal. Bioanal. Chem.*, 387(6):2131–2141, 2007.

[103] F. Gao, L. Wang, L. Tang, and C. Zhu. A novel nano–sensor based on rhodamine-beta-isothiocyanate–doped silica nanoparticle for pH measurement. *Microchim. Acta*, 152:131–135, 2005.

[104] I. E. Borissevitch, T. T. Tominaga, H. Imasato, and M. Tabak. Protonation of porphyrins in liquid PVC membranes: effects of anionic additives and application to pH–sensing. *J. Lumin.*, 69:65–76, 1996.

[105] D. B. Papkovsky, G. V. Ponomarev, and O. S. Wolfbeis. Protonation of porphyrins in liquid PVC membranes: effects of anionic additives and application to pH–sensing. *J. Photochem. Photobiol. A*, 104:151–158, 1997.

[106] C. D. Natale, A. Macagnano, S. Nardis, R. Paolesse, C. Falconi, E. Proietti, P. Siciliano, R. Rella, A. Taurino, and A. D'Amico. Comparison and integration of arrays of quartz resonators and metal–oxide semiconductor chemoresistors in the quality evaluation of olive oils. *Sens. Act. B*, 78:303–309, 2001.

[107] J. A. J. Brunink, C. Di Natale, F. Bungaro, F. A. M. Davide, A. D'Amico, R. Paolesse, T. Boschi, M. Faccio, and G. Ferri. The application of metalloporphyrins as coating material for quartz microbalance–based chemical sensors. *Anal. Chim. Acta*, 325:53–64, 1996.

[108] R. Rella, P. Siciliano, L. Valli, K. Spaeth, and G. Gauglitz. An ellipsometric study of LB films in a controlled atmosphere. *Sens. Act. B*, 48:328–332, 1998.

[109] A. D. F. Dunbar, S. Brittle, T. H. Richardson, J. Hutchinson, and C. A. Hunter. Detection of volatile organic compounds using porphyrin derivatives. *J. Phys. Chem. B*, 114(36):11697–11702, 2010.

[110] O. Griesbeck, G. S. Baird, R. E. Campbell, D. A. Zacharias, and R. Y. Tsien. Reducing the environmental sensitivity of Yellow Fluorescent Protein. *J. Biol. Chem.*, 276(31):29188–29194, 2001.

[111] G. T. Hanson, T. B. McAnaney, E. S. Park, M. E. P. Rendell, D. K. Yarbrough, S. Chu, L. Xi, S. G. Boxer, M. H. Montrose, and S. J. Remington. Green Fluorescent Protein variants as ratiometric dual emission pH sensors. 1. structural characterization and preliminary application. *Biochemistry*, 41:15477–15488, 2002.

[112] B. G. Abraham, N. V. Tkachenko, V. Santala, H. Lemmetyinen, and M. Karp. Bidirectional Fluorescence Resonance Energy Transfer (FRET) in mutated and chemically modified Yellow Fluorescent Protein (YFP). *Bioconjugate Chem.*, 22(2):227–234, 2011.

[113] M. Elsliger, R. M. Wachter, G. T. Hanson, K. Kallio, and S. J. Remington. Structural and spectral response of Green Fluorescent Protein variants to changes in pH. *Biochemistry*, 38(17):5296–5301, 1999.

[114] K. Truong, A. Sawano, A. Miyawaki, and M. Ikura. Calcium indicators based on Calmodulin–fluorescent protein fusions. *Methods Mol. Biol.*, 352:71–82, 2007.

[115] J. Nakai, M. Ohkura, and K. Imoto. A high signal–to–noise Ca^{2+} probe composed of a single Green Fluorescent Protein. *Nat. Biotechnol.*, 19:137–141, 2001.

[116] J. S. Lindsey and R. W. Wagner. Investigation of the synthesis of ortho–substituted tetraphenylporphyrins. *J. Org. Chem.*, 54(4):828–836, 1989.

[117] *HC19-1550-01, Hollow Core Photonic Bandgap Fiber Datasheet.* URL `http://www.nktphotonics.com/files/files/HC19-1550-01-100409.pdf`.

[118] E. Sariola-Leikasa, M. Hietalaa, A. Veselov, O. Okhotnikov, S.L. Semjonov, N.V. Tkachenko, H. Lemmetyinen, and A. Efimov. Synthesis of porphyrinoids with silane anchors and their covalent self-assembling and metallation on solid surface. *J. Colloid Interf. Sci.*, 2011, submitted.

[119] N. V. Tkachenko. *Optical Spectroscopy Methods and Instrumentations.* Elsevier, Amsterdam, 2006.

[120] M. Anikin, N. V. Tkachenko, and H. Lemmetyinen. Arrangement of a hydrophobically shielded porphyrin, 5,10,15,20-tetrakis(3,5-di-tert-butylphenyl)porphyrin, in octadecylamine Langmuir–Blodgett multilayers. *Langmuir*, 13:3002–3008, 1997.

[121] D. Gust, T. A. Moore, A. L. Moore, D. K. Luttrull, J. M. DeGraziano, N. J. Boldt, M. Van der Auweraer, and F. C. De Schryver. Tetraarylporphyrins in mixed Langmuir–Blodgett films: steady–state and time–resolved fluorescence studies. *Langmuir*, 7:1483–1490, 1991.

[122] D. M. Togashi, R. I. S. Romao, A. M. Goncalves da Silva, A. J. F. N. Sobral, and S. M. B. Costa. Self–organization of a sulfonamido–porphyrin in Langmuir monolayers and Langmuir–Blodgett films. *Phys. Chem. Chem. Phys.*, 7:3874–3883, 2005.

[123] D. G. Kurth and T. Bein. Surface reactions on thin layers of silane coupling agents. *Langmuir*, 9:2965–2973, 1993.

[124] Y. Z. Du, L. L. Wood, and S. S. Saavedra. Growth behavior and structure of alkyltrichlorosilane monolayers bearing thioacetate and acetate tailgroups. *Mater. Sci. Eng.*, 7:161–169, 2000.

[125] P. J. Goncalves, L. De Boni, N. M. Barbosa Neto, J. J. Rodrigues, S. C. Zilio, and I. E. Borissevitch. Effect of protonation on the photophysical properties of meso-tetra(sulfonatophenyl)porphyrin. *Chem. Phys. Lett.*, 407:236–241, 2005.

[126] E. B. Fleischer. The structure of porphyrins and metalloporphyrins. *Acc. Chem. Res.*, 3:105–112, 1970.

[127] F. Yang, L. G. Moss, and G. N. Phillips. The molecular structure of Green Fluorescent Protein. *Nat. Biotechnol.*, 14:1246–1251, 1996.

[128] M. Ormö, A. B. Cubitt, K. Kallio, L. A. Gross, R. Tsien, and S. J. Remington. Crystal structure of the Aequorea victoria Green Fluorescent Protein. *Science*, 273:1392–1395, 1996.

[129] K. M. Alkaabi, A. Yafea, and S. S. Ashraf. Effect of pH on thermal– and chemical–induced denaturation of Green Fluorescent Protein (GFP). *Appl. Biochem. Biotechnol.*, 126:149–156, 2005.

[130] D. Kuciauskas, S. Lin, G. R. Seely, A. L. Moore, T. A. Moore, D. Gust, T. Drovetskaya, C. A. Reed, and P. D. W. Boyd. Energy and photoinduced electron transfer in porphyrin-fullerene dyads. *J. Phys. Chem.*, 100:15926–15932, 1996.

Papers I–V

Papers I–V

Paper I

Photochemical properties of porphyrin films covering curved surfaces of optical fibers.

A. Veselov; C. Thür; V. Chukharev; M. Guina; H. Lemmetyinen; N.V. Tkachenko.

Chem. Phys. Lett., *471*: 290–294, **2009**.

Paper II

Photochemical properties of porphyrin films covering surfaces of tapered optical fibers.

A. Veselov; C. Thür; V. Chukharev; M. Guina; H. Lemmetyinen; N.V. Tkachenko.

Proc. of SPIE, *7503*: 75031K–75031K4, **2009**.

Paper III

Acidity sensor based on porphyrin self-assembled monolayers covalently attached to the surfaces of tapered fibres.

A. Veselov; C. Thür; A. Efimov; M. Guina; H. Lemmetyinen; N.V. Tkachenko.

Meas. Sci. Technol., *21*: 115205–115215, **2010**.

Paper IV

Self-assembled monolayers (SAMs) of porphyrin deposited inside photonic crystal fibre (PCF).

A. Veselov; C. Thür; A. Efimov; M. Guina; H. Lemmetyinen; N.V. Tkachenko.

Phys. Status Solidi A, *208 (8)*: 1858–1861, **2011**.

Paper V

Photochemical properties and sensor applications of modified Yellow Fluorescent Protein (YFP) covalently attached to the surfaces of etched optical fibres (EOFs).

A. Veselov; B.G. Abraham; M. Karp; H. Lemmetyinen; N.V. Tkachenko.

Anal. Bioanal. Chem., submitted.
